Recovery of vortex packet organization in perturbed turbulent boundary layers

Yan Ming Tan and Ellen K. Longmire
Department of Aerospace Engineering and Mechanics, University of Minnesota, Minneapolis 55455, USA
(Received 14 December 2016; published 12 October 2017)

Turbulent boundary layers with $\mathrm{Re}_\tau = 2500$ were perturbed by an array of cylinders projecting outward from the wall, and the flow organization downstream was investigated at multiple measurement heights in the logarithmic region. Two array heights were considered: $H = 0.2\delta$, extending through the log region and $H = \delta$, extending to the top of the boundary layer. Results from instantaneous PIV in wall-parallel planes and a vortex packet identification algorithm clearly showed a bottom-up mechanism for packet recovery downstream of the $H = \delta$ array, even though streamwise velocity statistics remained strongly perturbed. In contrast, some indications of top-down recovery were observed for the flow perturbed by the shorter $H = 0.2\delta$ ($H^+ = 500$) array. In this case, however, packet structures closer to the wall at $z^+ = 125$ remained altered beyond the end of the measurement domain 7δ downstream of the cylinders even though streamwise velocity statistics relaxed nearly to the unperturbed values.

DOI: 10.1103/PhysRevFluids.2.104602

I. INTRODUCTION

Based on extensive PIV measurements acquired at multiple Reynolds numbers, Adrian *et al.* [1] argued that individual hairpin vortices within turbulent boundary layers (TBLs) were frequently organized and convected in streamwise-aligned groups or packets. Here, we use the term hairpins to include canes, arch, and asymmetric shapes following Adrian *et al.* [1]. Aspects of hairpin packet organization and dynamics have since been investigated in many additional studies [2–11]. Adrian *et al.* [1] hypothesized that the organization of hairpins into packets enhances the Reynolds stresses produced through cooperative transfer of momentum between the hairpin legs. This argument was supported by the work of Ganapathisubramani *et al.* [9], who found that regions associated with packets contributed substantially to the Reynolds stress despite occupying a relatively small area. Furthermore, vortex packets were demonstrated to be statistically significant within boundary layers through the successful reproduction of single and multipoint boundary layer statistics [12–14] based on the attached eddy hypothesis [15,16].

Studies on the mechanisms leading to the formation of packets include experiments by Smith *et al.* [17] and computations by Zhou *et al.* [18,19] and Kim *et al.* [20], which showed that a sufficiently strong perturbation results in a hairpin that can spawn additional hairpins upstream and downstream. This mechanism is known as auto-generation. More recently, Jodai and Elsinga [11] presented time-resolved tomographic PIV results showing a hairpin packet forming from near-wall quasistreamwise vortices and new hairpins induced by existing packets.

Multiple studies have shown that smaller hairpins may reorganize through vortex-reconnection and annihilation mechanisms to form structures of larger scale [17,21,22]. Tomkins and Adrian [23] found that spanwise scales associated with packets in the logarithmic region of a boundary layer grew linearly with increasing wall-normal distance, indicative of self-similar growth. The authors hypothesized that vortex reconnection and annihilation provided a means for smaller packets initiating closer to the wall to form larger ones that extended further from the wall. This mechanism manifested in their data as merging of spanwise neighboring packet regions into wider ones.

By contrast, large-scale motions, e.g., long low-momentum regions in the outer layer of a TBL have been shown to affect the near wall region [24,25]. In particular, the large-scale motions in the outer layer modulated the amplitude of small scale fluctuations close to the wall [26–29].

 ©2017 American Physical Society

Wall roughness has been investigated extensively as a means of perturbing boundary layer organization. Typically, the roughness elements are much smaller than the boundary layer thickness, and distributed over a significant streamwise distance (e.g., Refs. [30–35]). Some studies have employed a relatively sparse arrangement of the roughness elements (e.g., Refs. [31,36–39]). In general, the effects of the roughness were confined to the inner layer, such that coherent structures in the outer flow resembled those in smooth-wall boundary layers (e.g., Refs. [40,41]).

The present study differs from rough wall studies in that it considers only a single array of perturbing elements that protrude farther into the boundary layer to affect larger eddies within the flow. Many previous experiments on large eddy break-up (LEBU) devices fall into this category (e.g., Refs. [42–46]). In general, LEBU devices were shown to reduce skin friction drag downstream, with the effect lasting up to 150 times the boundary layer thickness [45]. The suppression of large-scale motions within the boundary layer, resulting from interaction of the wakes from the LEBU devices with pre-existing turbulent eddies, was proposed as a potential mechanism leading to the skin friction reduction [46,47].

A number of previous experiments have documented changes in averaged velocity statistics downstream of relatively porous but tall obstructions. Corke *et al.* [42] examined the flow downstream of four wall-parallel plates with narrower wall-normal spacing closer to the wall. The flat plate manipulators extended to 0.8δ where δ is the boundary layer thickness, although remaining fairly porous at 4% frontal blockage to the oncoming boundary layer ($\mathrm{Re}_\tau \sim 1900$). Their hot-wire results showed a deficit in streamwise velocity relative to the unperturbed flow for $z < 0.5\delta$ and reduced streamwise root-mean square (RMS) velocities for $z/\delta < 0.1$ up to $\sim 9\delta$ downstream of the manipulators, where z is the wall-normal coordinate. They attributed the reduced RMS values to the inhibition of wall-normal velocity fluctuations, impeding flow interactions across the depth of the boundary layer. Boiko and Kornilov [48] observed a similar effect in experiments within the log region of a boundary layer perturbed by an array of vertically oriented wall-mounted flat plates ($H/\delta = 0.5$, blockage $= 22\%$), spaced 0.2δ apart. The reduction in streamwise RMS velocity lasted up to 7δ downstream, which was their last measurement location. Hutchins and Choi [49] also observed reductions in streamwise RMS velocities within the log region up to 7δ downstream of two streamwise aligned vertical plates spaced at 0.2δ and extending to $H/\delta = 0.5$. Separately, Lee *et al.* [50] studied the flow downstream of a two-dimensional (2D) fence with 65% porosity, extending to a height $H/\delta \sim 10$. They observed a sustained deficit in streamwise velocity for $z/\delta < 1$ up to the last measurement location 7.5δ downstream. Other studies with obstacles of limited streamwise extent and relatively large height have also shown a strong influence on the organization of the flow structures downstream (e.g., Refs. [51,52]).

Studies related to sparse obstructions with limited height compared to δ include those of Tomkins [53] and Guala *et al.* [54]. They examined the effects of periodic arrays of wall-mounted hemispheres ($H/\delta = 0.09$) on the packet organization in the outer layer, and saw a reduction in the streamwise length scales of the packets. Furthermore, the inclination angles of packet signatures steepened in regions beyond the height of the perturbation. Jacobi and McKeon [55] saw that four 2D spanwise bars ($H/\delta = 0.06$) staggered in the streamwise direction redistributed the population of swirls in the wall-normal direction, increasing the number at $z/\delta = 0.2{-}0.3$, while decreasing the population of swirls closer to the wall. Moreover, they observed a velocity deficit immediately downstream of the perturbation for $z/\delta < 0.3{-}0.4$, which persisted over a distance of 15δ. They also observed an increase in streamwise RMS velocities, with a peak at the bar height immediately downstream of the perturbation that decayed in strength and propagated away from the wall with increasing streamwise distance.

The present work considers a spanwise array of cylinders with spacing of 0.2δ. Previously, Zheng and Longmire [56] investigated the effects of a similar array with height $H = 0.2\delta$ ($H^+ = 500$) on packet organization using stereoscopic PIV and flying PIV. In measurement planes at $z^+ = 300$, packets were disrupted immediately downstream of this array, where wakes with Karman-like shedding patterns appeared directly behind each cylinder pair. The individual wakes interacted strongly with one another in the spanwise direction resulting in highly disorganized flow downstream

as well as a shift of the mean velocity deficit into the regions midway between cylinders (see also Ref. [57]). Also, on average, flow was induced to move toward the wall in the cylinder wakes by structures shedding off of the cylinder tips and away from the wall in the mid-span between each cylinder, resulting in a highly three-dimensional (3D) flow on average [58]. The flying PIV measurements at $z^+ = 300$ frequently showed the re-emergence of the incoming packet organization beginning about 2δ downstream of the array. Based on this result, Zheng and Longmire [56] hypothesized that the recovery of previously existing packet signatures was due to the unperturbed packet organization above the array propagating toward the wall. This idea is consistent with the result of modulation of near wall structures by larger scales in the outer layer [25,26,28].

The objective of the current paper is to investigate mechanisms of packet recovery downstream of similar arrays considering multiple array and measurement heights. Specifically, an array height extending to the edge of the boundary layer thickness ($H = \delta$) is included with the goal of completely eliminating the pre-existing packet organization. Packet recovery is investigated qualitatively through examination of individual PIV fields and quantitatively through the application of a vortex packet identification algorithm.

Previous studies using feature extraction algorithms to extract packet-like structures or low momentum zones within boundary layers include those of Ganapathisubramani *et al.* [9] and Lin *et al.* [59]. The former work employed a region-growing algorithm on stereoscopic PIV data in wall parallel planes to extract packet signatures. Regions with large Reynolds stress bounded by strips of positive and negative wall-normal vorticity were used as seed points. Then, neighboring points within a specified range of streamwise velocity were connected such that the final identified region had a relatively uniform (and low) streamwise momentum. Finally, neighboring regions separated by streamwise distance less than their average widths were merged. Lee and Sung [60] modified the aforementioned algorithm to specifically extract large (long) and very large-scale features in their simulated boundary layer. Lin *et al.* [59], on the other hand, employed an algorithm to extract regions of low and high streamwise momentum in the buffer region. Thresholds dependent on the standard deviation of the streamwise velocity were employed to define coherent regions which were subsequently refined by erosion and dilation of the binarized images. In a separate study, Nolan and Zaki [61] used a feature detection algorithm to track and acquire amplitudes of streaks in DNS results of a transitional boundary layer.

In this paper, we present an improved feature detection algorithm compared with an earlier version described in Tan and Longmire [62]. The algorithm employs aspects of multiple features to detect and extract individual vortex packet signatures in both unperturbed and perturbed velocity fields derived from planar PIV measurements.

II. EXPERIMENTAL FACILITIES & METHODS

All experiments were performed in the water channel facility at the Department of Aerospace Engineering & Mechanics, University of Minnesota. The test section of the channel measures 8 m long and 1.22 m wide. The water free surface sits 0.39 m above the bottom wall. The flow is driven by three propellers located beneath the end of the test section where recirculation occurs from outlet to the inlet. Prior to the inlet of the test section, the flow goes through a series of honeycomb and screens followed by an asymmetric 5:1 contraction. A 3-mm circular trip-wire is located at the entrance to the channel test section, followed by boundary layer development along the bottom wall. At a distance 6 m downstream of the trip, the boundary layer height was $\delta = 125$ mm, and $\mathrm{Re}_\tau = 2500$ with a freestream velocity, $U_\infty = 0.508$ m/s. The free stream turbulence intensity was evaluated to be $0.014U_\infty$ [63]. Further details on the facility and base flow parameters can be found in Gao [63].

The PIV measurement system included a dual-head Spectra Physics Nd:YAG laser capable of 370 mJ/pulse and two 12-bit TSI 4MP PowerView Cameras with 2048×2048 pixels, which were aligned to obtain a relatively wide field of view. Nikon Micro-Nikkor 60-mm lenses were used with f number of 11, resulting in a magnification of 0.1. Both cameras were angled slightly to provide

some spanwise overlap between the individual fields of view and were equipped with Scheimpflug adapters. The resulting field of view was $1.1\delta \times 2.2\delta$ in the streamwise (x) and spanwise (y) directions, respectively. The optics for beam shaping included multiple mirrors, two spherical lenses with focal length $f = 1000$ mm and $f = 500$ mm, respectively, then two convex cylindrical lenses with $f = 60$ mm to produce the final light sheet, which was roughly 1 mm in thickness. The flow was seeded with silver coated hollow glass spheres with an average diameter of 13 μm. The imaged particles were typically larger than 3 pixels. The resolution of the PIV data was 2.2 mm or 40 wall units. Based on a 50% overlap, the vector spacing of the data was 1.1 mm or 20 wall units. At every measurement location, 1000 independent PIV fields were captured at a rate of 0.5 Hz. The time between paired laser pulses was 1800 μs, resulting in average particle displacements of 8 pixels in the unperturbed flow. The uncertainty in each component of the instantaneous PIV vectors was $0.012U_\infty$. The random uncertainty in streamwise velocity averaged over an entire set of data fields was negligible and less than $0.001U_\infty$ for all cases and measurement heights.

A spanwise array of cylinders was mounted at the streamwise location 6 m downstream of the trip wire with unperturbed boundary layer characteristics as given above. This streamwise location will be designated as $x = 0$ in subsequent discussion. The streamwise, spanwise, and wall-normal directions are denoted by x, y, and z, and U and V are the streamwise and spanwise velocity, respectively. Two array heights were considered: $H = 0.2\delta$ (or $H^+ = 500$) and $H = \delta$. The cylinder diameter was held constant at $D = 6.35$ mm. Cylinders, made of stainless steel, were spaced at 0.2δ in both arrays. The frontal blockage posed by the arrays as a percentage of the frontal area of the boundary layer at $x = 0$ was 5% for $H = 0.2\delta$ and 25% for $H = \delta$. PIV data were acquired at three measurement heights: $z^+ = 125$, $z^+ = 300$, and $z^+ = 500$, extending across the log region and six streamwise locations downstream of the array encompassing $0 \leqslant x/\delta \leqslant 7.5$. The growth of the unperturbed boundary layer over this distance was estimated to be roughly 10% of the boundary layer height at $x = 0$. The resulting change in measurement height at the field centered at $x/\delta = 7$ was estimated to be $z^+ = 122$, 295, and 491, respectively.

A. Vortex packet identification algorithm (VPIA)

As the vortex packet identification algorithm (VPIA) was to be used for comparison purposes, i.e., perturbed versus unperturbed flow, we sought to identify only "individual" packet signatures not complicated by spanwise merged or merging structures. In addition, packet signatures intersecting the spanwise edges of the PIV fields were not considered. Furthermore, the algorithm was devised to be restrictive, i.e., our strategy was to minimize false positives, rather than to identify every individual packet signature within the data. Under this restriction, we aimed to capture as many individual packet signatures as possible. Based on previous literature [9,23] and our experience analyzing many instantaneous streamwise-spanwise fields, we define packet signatures as coherent slow moving regions bounded by counter rotating swirls (signed by wall-normal vorticity direction). In this context, swirl or swirling strength is defined as the imaginary part of the eigenvalues of the two-component velocity gradient tensor [19] where in this case, swirling structures could be cross sections of hairpin necks or legs. The essence of the algorithm is to employ image processing functions to automatically extract and catalogue packets with criteria guided by our experience viewing many instances of packet signatures. The algorithm was conditioned based on packet signatures observed in unperturbed flow, then applied to both unperturbed and perturbed data.

The algorithm description is as follows:

Step 1: A threshold was applied to the PIV velocity data to identify regions of $U < 0.95\bar{U}$ where $\bar{U}$ is the mean velocity at the measurement height.

Step 2: The thresholded velocity field was binarized, and MATLAB image processing functions were used to detect connected regions. The resulting output corresponding to the sample field in Fig. 1(a) is shown in Fig. 1(b).

Step 3: Erosion and dilation were performed on the structures identified to separate weakly connected regions. The resulting output from this step is shown in Fig. 1(c).

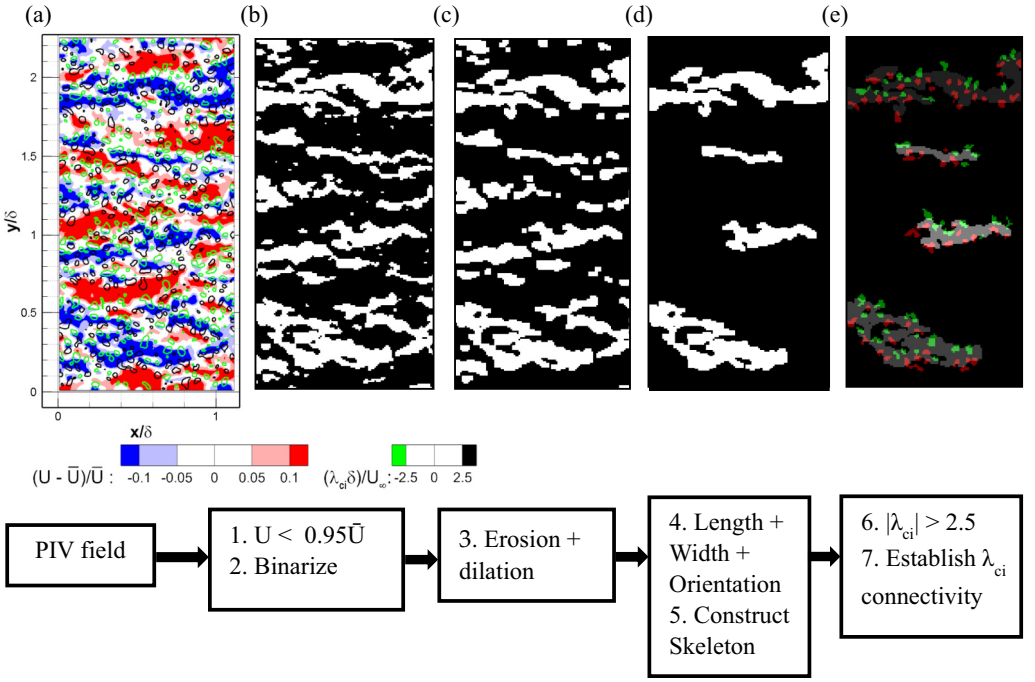

FIG. 1. VPIA process on a sample field. (a) Sample input to VPIA, intermediate outputs after (b) steps 1–2, (c) step 3, (d) steps 4–5, (e) steps 6–7.

Step 4: The length, width, and orientation of the detected regions were computed. The length and width were determined based on the streamwise and spanwise extrema of the detected region, respectively. The orientation was determined by fitting an ellipse to the outline of the structure, and taking the angle between the major axis and the streamwise direction. Minimum thresholds were set for the length (0.5δ) and width (0.05δ) in order to extract structures with significant streamwise and spanwise extent. The length threshold was designed to include structures with a minimum of about five hairpins based on streamwise spacing between hairpin heads reported by Adrian *et al.* [1]. The width threshold was based on the finding of Tomkins and Adrian [23] that coherent low speed regions at $z^+ = 100$ typically exceeded 0.04δ in width. Additionally, structures with large spanwise inclinations to the streamwise direction ($\beta > 25^\circ$) were removed as packet signatures in unperturbed flow tend to have little spanwise inclination (see, e.g., Tomkins and Adrian [23]). The output of Steps 1 through 4 applied to a sample unperturbed field is shown in Fig. 1(d).

Step 5: Streamwise scans of the remaining structures were performed in order to construct a skeleton. First, the width of the structure at every streamwise location was computed and averaged, to acquire an estimate of the mean width. Then, the skeleton was constructed by connecting regions for which the local width was greater than 50% of the mean width. Structures with large gaps in the skeleton (>245 wall units or 0.1δ) were removed as they did not look like packet signatures in the unperturbed flow. An example of a detected skeleton in unperturbed flow is shown in Fig. 2(a). Figure 2(b) shows an identified structure from perturbed flow that was removed due to the large gap in its skeleton.

Step 6: The swirling strength, λ_{ci}, was computed where the velocity gradients were obtained via central difference and normalized by the freestream velocity and δ. A threshold of $|\lambda_{ci}| > 2.5$ was applied, and the resulting swirl fields were binarized. This threshold was selected to suppress noise while retaining as many swirl structures as possible. Using similar connection and extraction methods as in steps 1–2, all swirling structures were separated and labeled. The minimum length

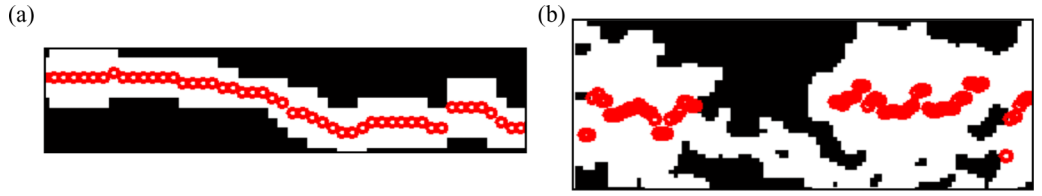

FIG. 2. Sample skeletons acquired from the streamwise scan of the structure width.

and width of the detected swirl structures was set at 3 grid points (75 wall units or 0.03δ) to suppress noise.

Step 7: Swirling regions that overlapped low momentum regions (LMRs) were identified. Prior to swirl identification, the low momentum regions were dilated with a rectangular kernel of length 5 (123 wall units) and width 3 grid points (75 wall units). The dilation allowed inclusion of swirling structures that were slightly offset from but still associated with the parent LMR. The number of swirls per length ($N_{s/L}$) and the ratio of positive to negative swirls ($N_{s+/s-}$) based on the sign of the wall-normal vorticity associated with each LMR were computed. Figure 1(e) shows all swirling structures that have been associated with the detected LMRs.

The steps described above were applied to sets of 100 PIV fields for unperturbed flow at all three measurement heights. Then, the structures identified were compared manually against the original PIV plots that overlaid swirling structures and streamwise velocity contours [e.g., Fig. 1(a)]. Structures identified by the algorithm were separated into the following categories: packets, nonpackets, merging/merged packets, and edge structures. The comparison revealed a number of false positives at each height. To decrease the number of false positives, threshold criteria based on $N_{s+/s-}$ and $N_{s/L}$ were added. The former helped eliminate structures that intersected the spanwise edges of the field, while the latter helped eliminate merged/merging structures. Additionally, both criteria were effective at eliminating some structures that lacked associated swirls. The threshold values can be found in Table I.

After applying these additional criteria at $z^+ = 125$ and $z^+ = 300$ in the unperturbed flow, no nonpackets were present in the VPIA output from the unperturbed data sets examined. On the other hand, 3% of the detected structures at $z^+ = 500$ were classified as nonpackets. At all measurement heights, a small number of structures detected were classified as merged/merging packets. These structures were difficult to remove as their statistics could closely resemble those of individual packet signatures. More restrictive thresholds on $N_{s/L}$ could exclude these structures but only at a cost of losing a greater number of individual packet signatures.

TABLE I. Values of thresholds applied to unperturbed and perturbed data at each measurement height.

Criteria	$z^+ = 125$	$z^+ = 300$	$z^+ = 500$
U	$<0.95\bar{U}$	$<0.95\bar{U}$	$<0.95\bar{U}$
L_{ex}	$>0.5\delta$	$>0.5\delta$	$>0.5\delta$
W_{ex}	$>0.05\delta$	$>0.05\delta$	$>0.05\delta$
β	$<25^\circ$	$<25^\circ$	$<25^\circ$
W_m	$<0.2\delta$	$<0.25\delta$	$<0.3\delta$
N_h	<4	<4	<4
AR	>2	>2	>1.5
A_h	>0.97	>0.97	>0.97
$N_{s+/s-}$	0.5–1.5	0.5–1.5	0.5–1.5
$N_{s/L}$	$(15-40)/\delta$	$(15-40)/\delta$	$(15-40)/\delta$
L_{sk}/L_{ex}	N/A	N/A	>0.77
S_c	N/A	N/A	>0.58

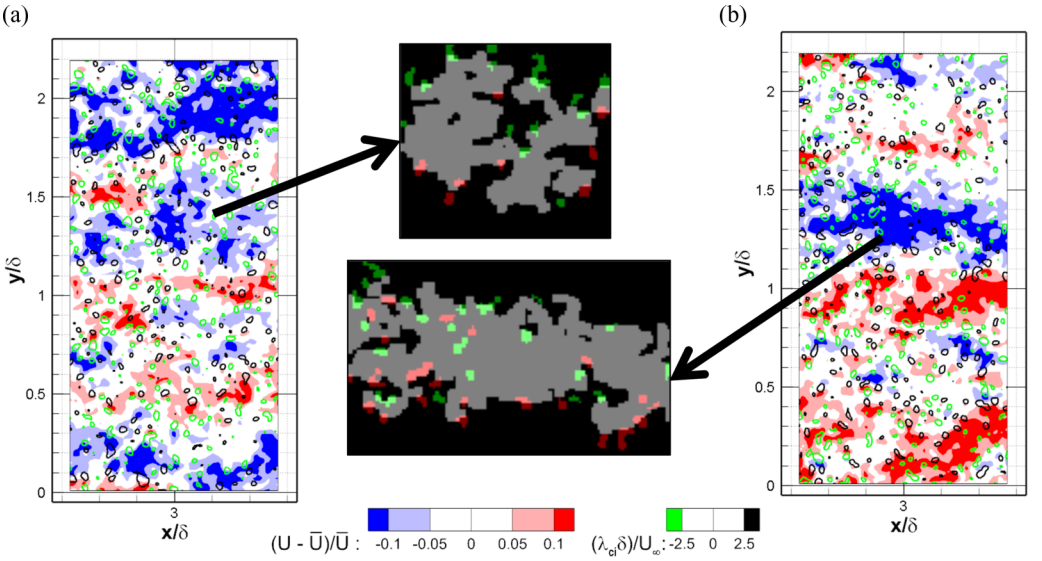

FIG. 3. Two samples of false detections behind $H = \delta$ array at $x/\delta = 2.9$, $z^+ = 500$. Green and red depict counter rotating swirls within the detected structures; gray contours show region associated with detected structure.

The algorithm, including the additional thresholds on $N_{s+/s-}$ and $N_{s/L}$, was next applied to the perturbed boundary layer data beginning at $x/\delta > 2.4$. The algorithm was not applied to locations with $x/\delta < 2.4$ as wakes from the cylinders could be dominant, and they were difficult to exclude from identification by the algorithm. To evaluate algorithm accuracy, the output of the algorithm and PIV data fields centered on $x/\delta = 2.9$ and $x/\delta = 7$ were compared manually, repeating the process followed for the unperturbed data. The comparison showed a large number of false positives associated with wakelike structures. Hence, additional criteria were devised based on examination of many samples. Generally, the false positives (or wakelike structures) tended to have the following visual characteristics:

(i) Many enclosed "holes" within structures caused by local zones of larger streamwise velocity
(ii) Many appendages attached to main structure
(iii) Significant width variation along the streamwise direction
(iv) Low aspect ratio
(v) Little obvious association between swirls on opposite sides of structure

Two examples of false positives from the perturbed data are shown in Fig. 3. The structure in Fig. 3(a) looks highly irregular and has a large width compared to its length. Furthermore, it lacks obvious swirl pairing. The structure in Fig. 3(b), which possibly results from spanwise merging packets, also lacks obvious swirl pairing. In addition, it includes seven holes. In order to filter out structures exhibiting the above characteristics, many criteria were examined, and amongst all criteria tested, the following were deemed most effective at minimizing false positives:

1. Convex solidity, S_c The ratio of the area of the structure over the area of the smallest possible convex polygon fitted to the outline of the structure. See Fig. 4.

2. N_h Number of enclosed holes within the structure.

3. A_h Ratio of the area of the structure over the area of the structure with holes filled.

4. L_{sk}/L_{ex} Sum of the lengths of identified skeleton segments divided by the distance between the streamwise extrema points.

5. Mean width, W_m The average of the widths measured at every streamwise location of the structure.

6. Aspect ratio (AR) Ratio of length to width based on extrema points.

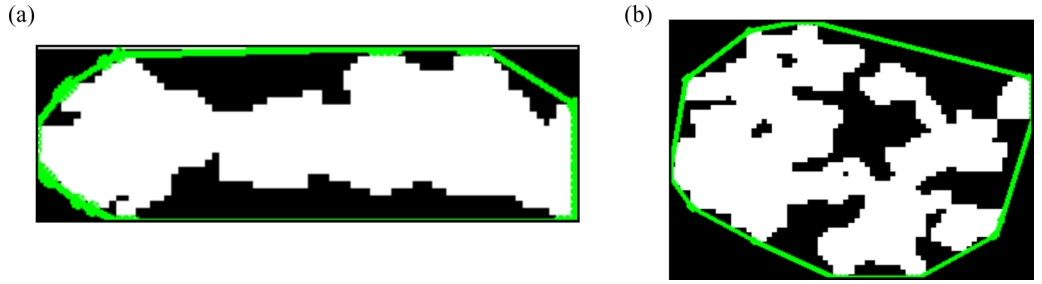

FIG. 4. Ratio of structure area (white) over area bounded by green line gives the measure of convex solidity. Two sample structures: (a) unperturbed, (b) perturbed.

The first three criteria (S_c, N_h, A_h) were selected to exclude structures with the first two characteristics (i and ii) listed above. These criteria, which are different measures of structure porosity, work better when applied together. For example, a structure with a single large hole would satisfy the N_h criterion, but would be excluded based on A_h. Meanwhile, the convex solidity measure would exclude a structure with multiple appendages [e.g., Fig. 3(a)], but no holes.

The skeleton length ratio (L_{sk}/L_{ex}) criterion was selected to exclude structures that vary substantially in local width but lack significant streamwise gaps in the skeleton. Recall that the skeleton is constructed only where the local width of the structure exceeds 50% of the mean width. For wavy structures typical of cylinder wakes, the local width can vary significantly over short streamwise intervals yielding short gaps in the skeleton. Therefore, this measure could exclude wavy structures with multiple short gaps (shorter than the threshold used in Step 5).

Separately, the mean width (W_m) was used to exclude structures that were merged or merging with spanwise adjacent structures. The aspect ratio (AR) also performs a similar function while also eliminating structures with lower aspect ratios than typical packet signatures in the unperturbed flow.

A large percentage of the false packet detections were eliminated with the above criteria. Those that remained still included the visual characteristics listed above (i–v). The threshold values could be adjusted to eliminate the remaining false detections, but only at a cost of eliminating many more real packet signatures.

The assigned thresholds for the above criteria are given in Table I. All thresholds were assessed for sensitivity. First, the basic criteria listed in Steps 1 and 4 ($\bar{U}$, L_{ex}, W_{ex}, β) were subjected to variations of 10% of their set threshold values in either direction. Then, the additional criteria ($N_{s+/s-}$, $N_{s/L}$, S_c, N_h, A_h, L_{sk}/L_{ex}, W_m, AR) were subjected to the same tests. Although the absolute numbers of identified packets varied with the threshold values, none of the threshold variations changed the trends in the results presented below.

Based on the assigned thresholds, tests were performed to ascertain statistical convergence for the number of packet signatures detected per field, $N_{p/f}$. Here, we define statistical convergence as being achieved when the variation of $N_{p/f}$ as the number of fields considered increases is bounded within an interval $\pm 2\%$ of the final value of $N_{p/f}$. The $N_{p/f}$ for short packets ($0.475\delta < L_{sk} < 0.525\delta$) was found to have statistically converged by $N = 300$, while $N_{p/f}$ for packets longer than the field of view ($L_{sk} > 1.05\delta$) converged by $N = 800$. On the other hand, the number of swirls per field, $N_{\lambda/f}$ was statistically converged by $N = 700$.

B. VPIA uncertainty

The results from the VPIA were subject to both bias error and random uncertainty. The bias error was due to over-counting from false positives. To assess over-counting, structures identified from VPIA with criteria in Table I applied were compared with those identified manually in 100 sample fields. False positives were identified and counted. The greatest number of false positives occurred

TABLE II. Uncertainty values for $N_{p/f}$ and $N_{\lambda/f}$ in the unperturbed flow at all measurement heights.

Case	Measurement height	$\delta N_{p/f}$	$\delta N_{p/f}$ (%)	$\delta N_{\lambda/f}$	$\delta N_{\lambda/f}$ (%)
Unperturbed	125	0.07	5.0%	0.74	0.2%
	300	0.05	5.6%	0.90	0.4%
	500	0.04	10.0%	0.81	0.5%

downstream of the $H = \delta$ array, $x/\delta = 2.9$, $z^+ = 500$, corresponding to 0.06/field. Typical values for other cases were 0.02/field.

Random uncertainty was determined for every case and streamwise location. In the unperturbed flow, the random uncertainties were 0.07/field at $z^+ = 125$, 0.05/field at $z^+ = 300$ and 0.04/field at $z^+ = 500$ at all streamwise locations. The random uncertainties for the perturbed flow were slightly larger. Downstream of the $H = \delta$ array, the random uncertainty was 0.09/field at $z^+ = 125$, 0.07/field at $z^+ = 300$ and 0.06/field at $z^+ = 500$. As for the $H = 0.2\delta$ array, the random uncertainties were 0.08/field at $z^+ = 125$, 0.07/field at $z^+ = 300$ and 0.07/field at $z^+ = 500$. The uncertainties affecting VPIA results for both unperturbed and perturbed flow are given in Tables II and III, respectively. Relative uncertainties for the perturbed flow were not included in Table III as values varied with cylinder height, measurement height, and streamwise location. The total uncertainty was assessed with the root mean sum of squares methodology to incorporate bias with random uncertainty, where in the vast majority of cases, the random uncertainty was dominant.

III. RESULTS

A. Unperturbed flow

Figure 5 shows sample plots from unperturbed flow obtained at the three measurement heights. The contour colors reflect slow (blue) and fast (red) moving regions relative to the local mean velocity of the measurement height. To recap, we consider a hairpin packet signature as a relatively long and narrow streamwise-coherent slow-moving region bounded by counter-rotating swirling structures (depicted by black and green contours). The packets observed at $z^+ = 125$ [Fig. 5(a)] were typically long and narrow, for example, at $y/\delta = 0.15$, 1.9, and possibly 1.6. At $z^+ = 300$ [Fig. 5(b)], the slow-moving zones became wider (e.g., $y/\delta = 0.3$, 0.8, and 1.6) and fewer swirling structures were observed. These trends continued at $z^+ = 500$ (e.g., Fig. 5(c), $y/\delta = 0.65$ and 1.2). Generally, packets tend to become wider and occasionally shorter with increasing height [23]. When the VPIA was applied to the unperturbed data (sets of 1000 fields), the results corroborated the aforementioned trends. The unperturbed number of packets per field, $N_{p/f}$ was greatest at $z^+ = 125$ (1.4/field) and decreased to 0.9/field at $z^+ = 300$ and 0.4/field at $z^+ = 500$.

TABLE III. Uncertainty values for $N_{p/f}$ and $N_{\lambda/f}$ in the perturbed flow at all measurement heights.

Case	Measurement height, z^+	$\delta N_{p/f}$	$\delta N_{\lambda/f}$
$H = \delta$	125	0.08	0.85
	300	0.07	0.83
	500	0.06	0.69
$H = 0.2\delta$	125	0.08	0.93
	300	0.07	0.84
	500	0.07	0.86

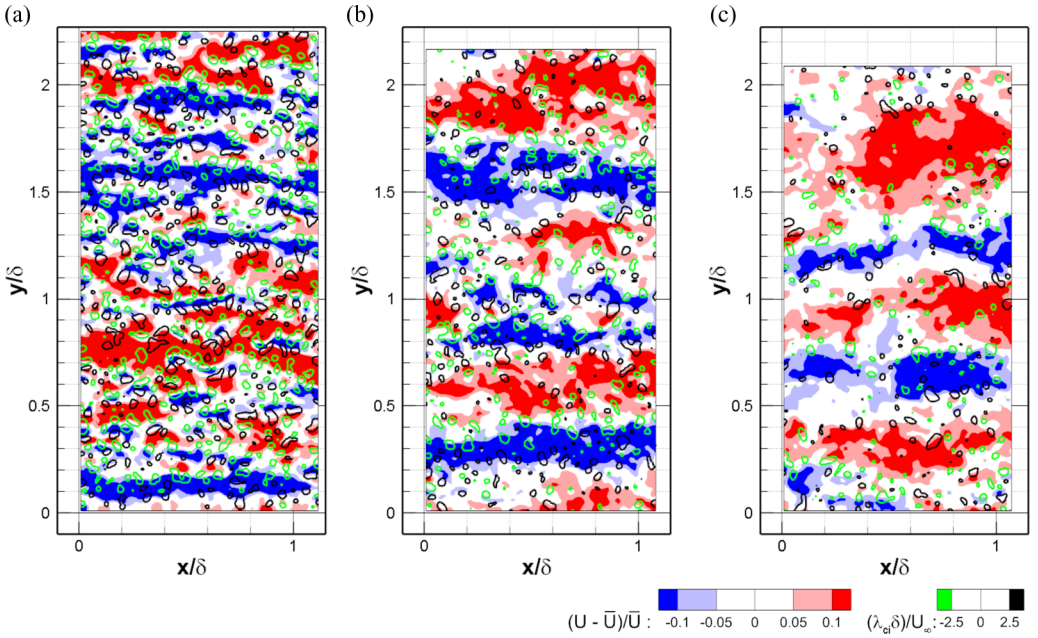

FIG. 5. PIV data of unperturbed flow at (a) $z^+ = 125$, (b) $z^+ = 300$, and (c) $z^+ = 500$. Blue and red contours show deviation from the local mean velocity at the measurement height.

The number of packets per field as a function of skeleton length is shown in Fig. 6(a). At each measurement height, the shape of the distribution is accurate for $L_{sk} < 1.025\delta$. Beyond this length, each distribution rises to a peak due to an aliasing effect since many packet signatures are longer than the field of view [see also 9,23]. The number of packets with length greater than the field of view (FOV) was largest at $z^+ = 125$ and least at $z^+ = 500$. Packet length distributions normalized by the number of packets detected at the local measurement height (not shown) yielded similar percentages of packets longer than the FOV at $z^+ = 125$ and 300 (22%), but a smaller percentage at $z^+ = 500$ (16%). Figure 6(b) shows the distribution of the mean widths of detected packets. With increasing wall-normal distance, the distribution becomes broader with the peak shifting toward larger values.

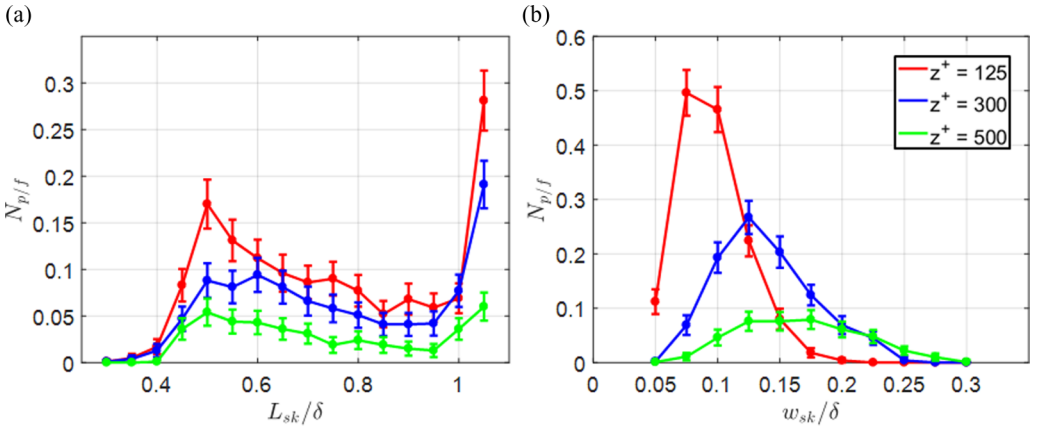

FIG. 6. Unperturbed flow. Number of packets per field as function of (a) packet skeleton length and (b) packet skeleton width. Histogram bin size = 0.05δ.

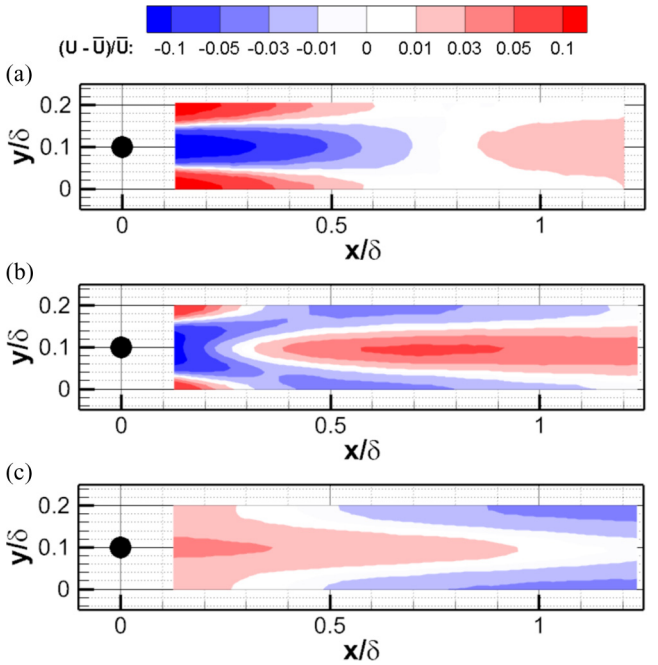

FIG. 7. Mean streamwise velocity downstream of flow perturbed by $H = 0.2\delta$ array at (a) $z^+ = 125$, (b) $z^+ = 300$, and (c) $z^+ = 500$.

The peak values of 0.075δ at $z^+ = 125$, 0.125δ at $z^+ = 300$ and possibly a peak at 0.15δ agree well with the findings of Tomkins and Adrian [23]. Here, the PIV field of view extended much wider than the distributions so no aliasing occurred.

B. Flow perturbed by array with $H = 0.2\delta$

The mean streamwise velocity immediately downstream of the $H = 0.2\delta$ cylinders, averaged over 1000 instantaneous fields and across nine cells along the spanwise dimension, is shown in Fig. 7. Each cell is centered on the cylinder axis and has a width of 0.2δ equal to the cylinder spacing. In these plots, random uncertainties in average velocity at each location are less than 1% of $\bar{U}$. Wakes occur behind each cylinder at both $z^+ = 125$ [Fig. 7(a)] and 300 [Fig. 7(b)]. Note that the length of the local momentum deficit becomes shorter with increasing wall-normal distance. At $z^+ = 500$ [Fig. 7(c)] or the cylinder tip height, fast moving zones form on average behind the cylinders. These fast-moving zones must result from local tip structures drawing faster moving fluid from above towards the wall (see, e.g., Refs. [58,64,65]). Wall-normal velocity measurements from stereoscopic PIV showed average downwash behind the cylinders at both $z^+ = 300$ and 500 (see Fig. 8, where measurements are averaged over four spanwise cells, and random uncertainties in average velocity at each location are 1% or less of $\bar{U}$). This downwash acts to split the averaged cylinder wakes at $z^+ = 300$, starting at $x = 0.2\delta - 0.3\delta$ [see Fig. 7(b)]. Averaged 3D PTV measurements (not shown) indicate that the localized downwash regions weakened to negligible average velocities by $z^+ = 155$ [66].

The mean and RMS streamwise velocity are plotted versus streamwise location in Fig. 9 for both unperturbed flow and flow downstream of the $H = 0.2\delta$ array. In all cases, the PIV results were averaged over streamwise-spanwise measurement fields centered on the plotted streamwise location. In the unperturbed flow, the mean and RMS velocity (U_{rms}) statistics matched well with DNS results at a comparable Reynolds number (Sillero *et al.* [67]), given the PIV resolution. We

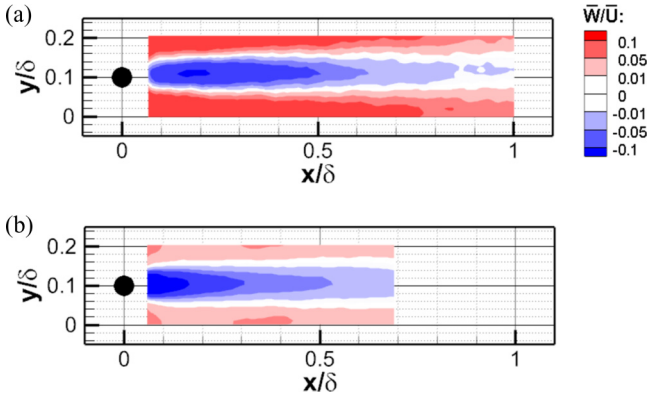

FIG. 8. Mean wall-normal velocity downstream of flow perturbed by $H = 0.2\delta$ array at (a) $z^+ = 300$ and (b) $z^+ = 500$.

estimate that all experimental RMS values were attenuated by 7% from the true values based on the work of Saikrishnan *et al.* [68].

In the perturbed flow, the mean streamwise velocity was reduced compared to the unperturbed flow at all measurement heights [Fig. 9(a)]. According to conservation of mass, the blockage posed by the $H = 0.2\delta$ array thus generates an average flow away from the wall. The decrease in streamwise velocity immediately downstream of the array was significant at 10% of free-stream velocity U_∞ for both $z^+ = 125$ and $z^+ = 300$ but much smaller (1%) at $z^+ = 500$, the cylinder tip height. Thus, it is likely that the upwash initiates closer to the wall and simply passes through the $z^+ = 500$ location at first. As x increased, however, the mean velocity at $z^+ = 500$ first decreased to a minimum between 2δ and 3δ before increasing gradually toward the unperturbed value. The decreasing trend likely results from the boundary layer profile adjusting to the sudden changes closer to the wall. At both $z^+ = 125$ and 300, the reduced mean velocity in the perturbed flow increased more rapidly towards the unperturbed value. At $x = 7\delta$, the streamwise velocity remained reduced by $2-3\%$ of U_∞ at all measurement heights compared to the values in the unperturbed flow.

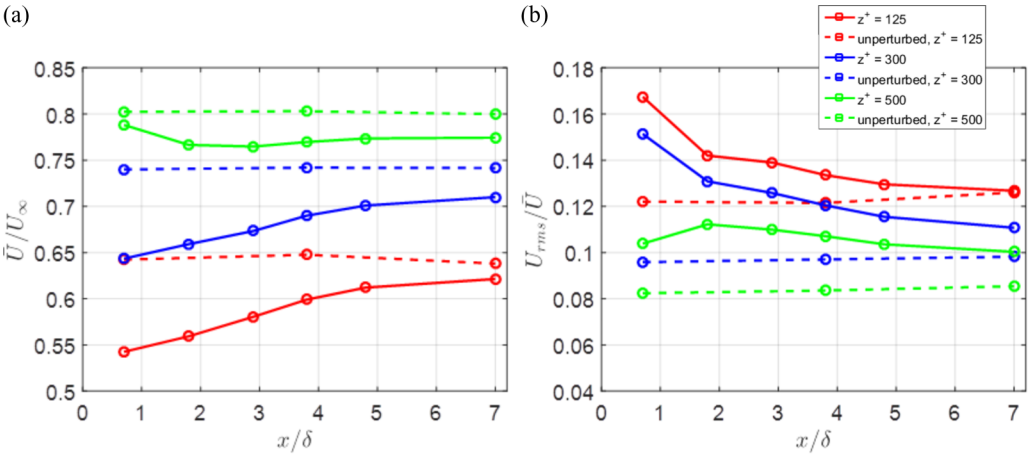

FIG. 9. Variation of (a) mean streamwise velocity normalized by free-stream velocity, and (b) root-mean square of streamwise velocity normalized with mean velocity at measurement height, with x location, downstream of the $H = 0.2\delta$ array.

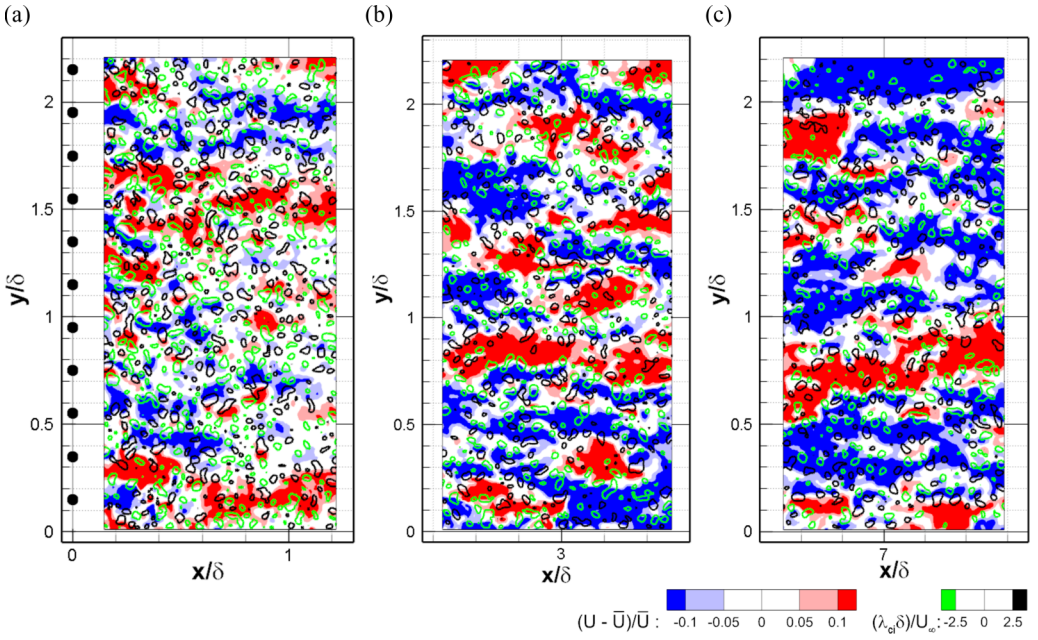

FIG. 10. PIV data of flow behind array with $H = 0.2\delta$ at $z^+ = 125$ centered at (a) $x = 0.7\delta$, (b) $x = 2.9\delta$, and (c) $x = 7\delta$.

The RMS velocity [Fig. 9(b)] increased significantly immediately downstream of the $H = 0.2\delta$ array at all measurement heights compared to the unperturbed values. The greatest relative increase occurred at $z^+ = 300$ ($0.05\bar{U}$), followed by $0.04\bar{U}$ at $z^+ = 125$ and $0.02\bar{U}$ at $z^+ = 500$, where $\bar{U}$ represents the mean value at the given measurement height. The RMS velocity at $z^+ = 500$ first increased to a maximum at $x = 1.8\delta$ before decreasing with increasing streamwise distance, while the RMS velocity decreased monotonically at the two locations closer to the wall. By $x = 7\delta$, the relative RMS velocity had recovered to the unperturbed value at $z^+ = 125$, but remained elevated by $0.01\bar{U}$ at $z^+ = 300$ and 500. The streamwise variations of spanwise RMS velocity (not shown) exhibited trends similar to those in streamwise RMS velocity shown in Fig. 9(b).

Instantaneous realizations of perturbed flow at $z^+ = 125$ and 300 revealed Karman like wake structures immediately downstream of the cylinders. No obvious packets were observed. If any were present, they were difficult to distinguish from the wakes. For $z^+ = 125$ [Fig. 10(a)], wakes can be observed at $y/\delta = 0.15$, 0.55, and 1.95. Similarly, for $z^+ = 300$ [Fig. 11(a)], wakes are observable at $y/\delta = 0.15$, 0.35, 0.55, and so on. Neighboring wakes often interact as seen at $y/\delta = 0.95$ and 1.15 in Fig. 11(a) for $z^+ = 300$, and $y/\delta = 1.75$ and 1.95 in Fig 10(a) at $z^+ = 125$. In spanwise regions between the cylinders, fast moving fluid was observed frequently, for example $y/\delta = 1.65$ at $z^+ = 125$ [Fig. 10(a)] and $y/\delta = 0.45$ for $z^+ = 300$ [Fig. 11(a)]. Wake structures were also dominant in the fields centered at $x = 1.8\delta$ (not shown).

At the array tip height ($z^+ = 500$), by contrast, we know from previous flying PIV measurements [62] that incoming packet signatures persisted through the array and continued to convect downstream. Also, wakes occurred less frequently directly behind the cylinders [see Fig. 12(a)]. More often, regions faster than the mean velocity were found in those locations, for example, at $y/\delta = 0.75$, 1.35, and 2. These regions might be caused by downwash downstream of cylinder tips drawing faster moving fluid from above towards the wall (see also the visualization of Park and Lee [65]). At this height, packet signatures were frequently observed directly downstream of the array as at $y/\delta = 1.15$ and 1.7 in Fig. 12(a). With increasing x, packet signatures continued to be observed,

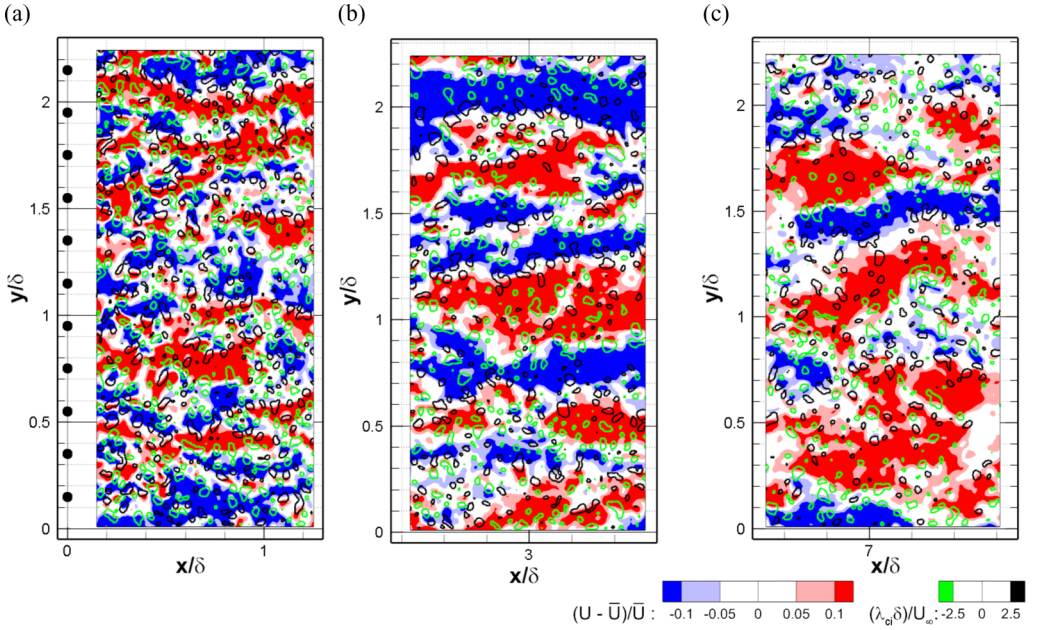

FIG. 11. PIV data of flow behind array with $H = 0.2\delta$ at $z^+ = 300$ centered at (a) $x = 0.7\delta$, (b) $x = 2.9\delta$, and (c) $x = 7\delta$.

for example, at $x = 2.9\delta$ [Fig. 12(b)] at $y/\delta = 0.3$ and 1.5, and at $x = 7\delta$ [Fig. 12(c)] at $y/\delta = 0.4$ and possibly 1.2 and 1.8.

At $z^+ = 300$, packets similar to those in the unperturbed flow were not apparent until 2.9δ downstream of the $H = 0.2\delta$ array, for example at $y/\delta = 1.3$ and 2.1 in Fig. 11(b). With increasing

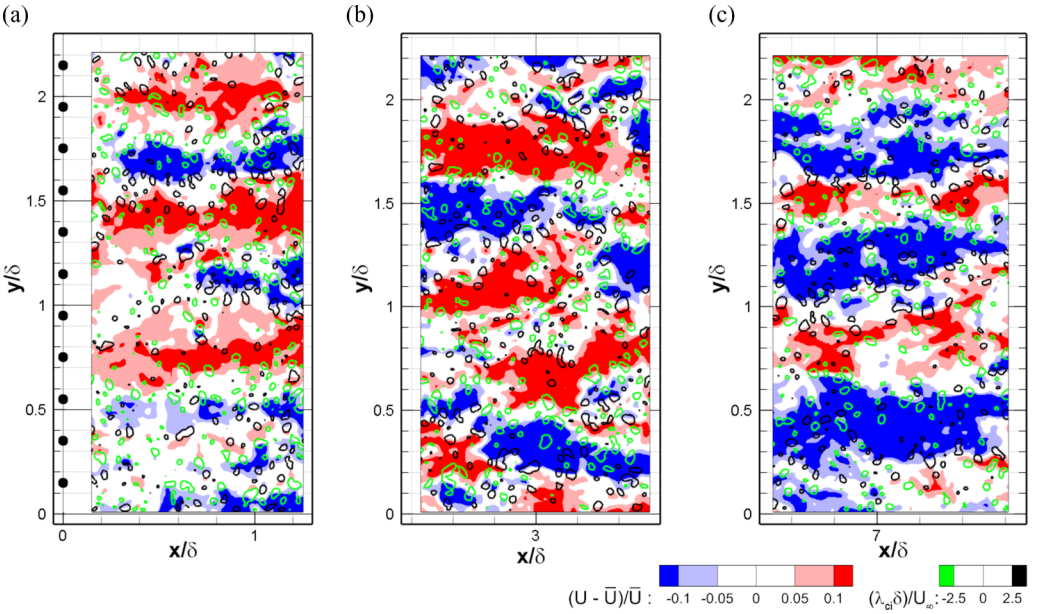

FIG. 12. PIV data of flow behind array with $H = 0.2\delta$ at $z^+ = 500$ centered at (a) $x = 0.7\delta$, (b) $x = 2.9\delta$, and (c) $x = 7\delta$.

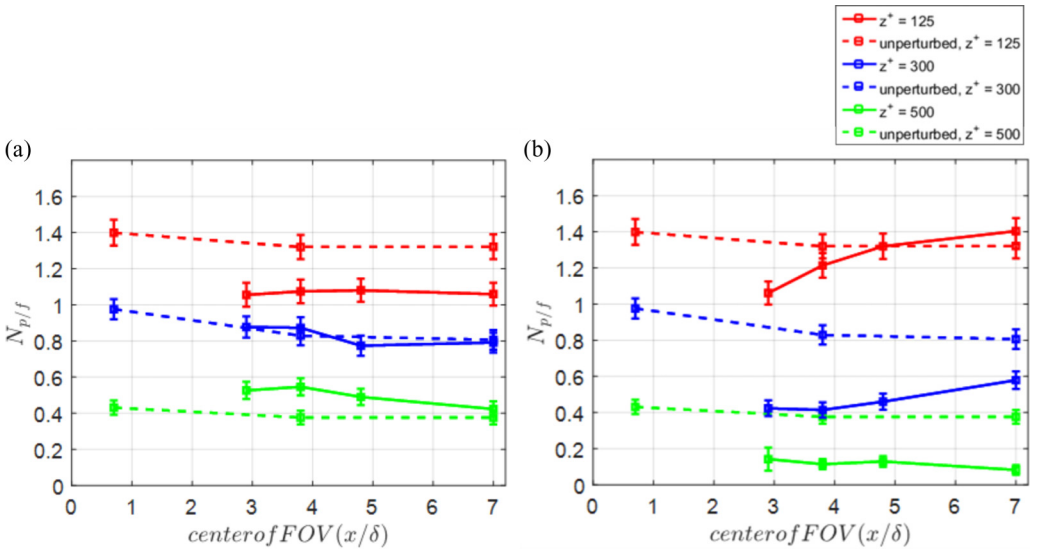

FIG. 13. Number of individual packets per field across three measurement heights for arrays with (a) $H = 0.2\delta$ and (b) $H = \delta$. The unperturbed counts are shown in dashed lines.

x, packets became even more like those observed in the unperturbed flow, i.e., their forms became less undulating. Examples of these are shown in Fig. 11(c) at $y/\delta = 1.5$.

At $z^+ = 125$, in contrast, low momentum structures at $x = 2.9\delta$ appeared wavy and unlike packet signatures in the unperturbed flow. Frequently, these wavy structures were connected to spanwise adjacent ones, as seen at $y/\delta = 0.3$ in Fig. 10(b). Wavy low momentum structures were still observed at $x/\delta = 7$, although they appeared less undulating compared with those at $x/\delta = 2.9$. In addition, many spanwise merged or merging structures were still observed. Examples of wavy and merged structures can be seen at $y/\delta = 0.4$, 1.1, and 1.6 in Fig. 10(c). Thus, the $H = 0.2\delta$ array was effective at enhancing and sustaining spanwise interactions between adjacent coherent zones of uniform streamwise velocity at $z^+ = 125$.

The number of packets per field identified by the VPIA as a function of streamwise location is shown in Fig. 13(a). For flow downstream of the $H = 0.2\delta$ array, the VPIA was not applied at the first two streamwise locations where wake structures were dominant [as in Figs. 10(a) and 11(a)]. At $z^+ = 125$, the number of packets was reduced at all streamwise locations examined up to $x/\delta = 7$. Over this streamwise range, the number per field was reduced by about 20% of the unperturbed value, where the reduction may stem from the increased frequency of merging/merged structures that were excluded by the VPIA. The curve at $z^+ = 300$ already reverted to the unperturbed curve starting at $x = 2.9\delta$. In contrast, at $z^+ = 500$, the packet count first increased, then relaxed to the unperturbed values with increasing streamwise distance. The relative increase was 40% of the unperturbed packet count at $z^+ = 500$. The reason for this increase was difficult to determine from the instantaneous fields. One reason may be that additional low momentum zones induced downstream of the cylinders extended upward by $x = 2.9\delta$.

Packet skeleton length distributions for flow downstream of the $H = 0.2\delta$ array are plotted in Figs. 14(a)–14(c) and compared against the unperturbed distributions. At $z^+ = 125$ [Fig. 14(a)], packet counts of all length scales were reduced initially and remained so until the last measurement location. In contrast, at both $z^+ = 300$ [Fig. 14(b)] and $z^+ = 500$ [Fig. 14(c)], the number of shorter packets increased initially. With increasing x, the distributions for both $z^+ = 300$ and 500 reverted toward the unperturbed distribution shape and values.

Figure 15(a) shows the total number of swirling structures identified downstream of the $H = 0.2\delta$ array at each measurement height where we assume that these structures represent cross sections of

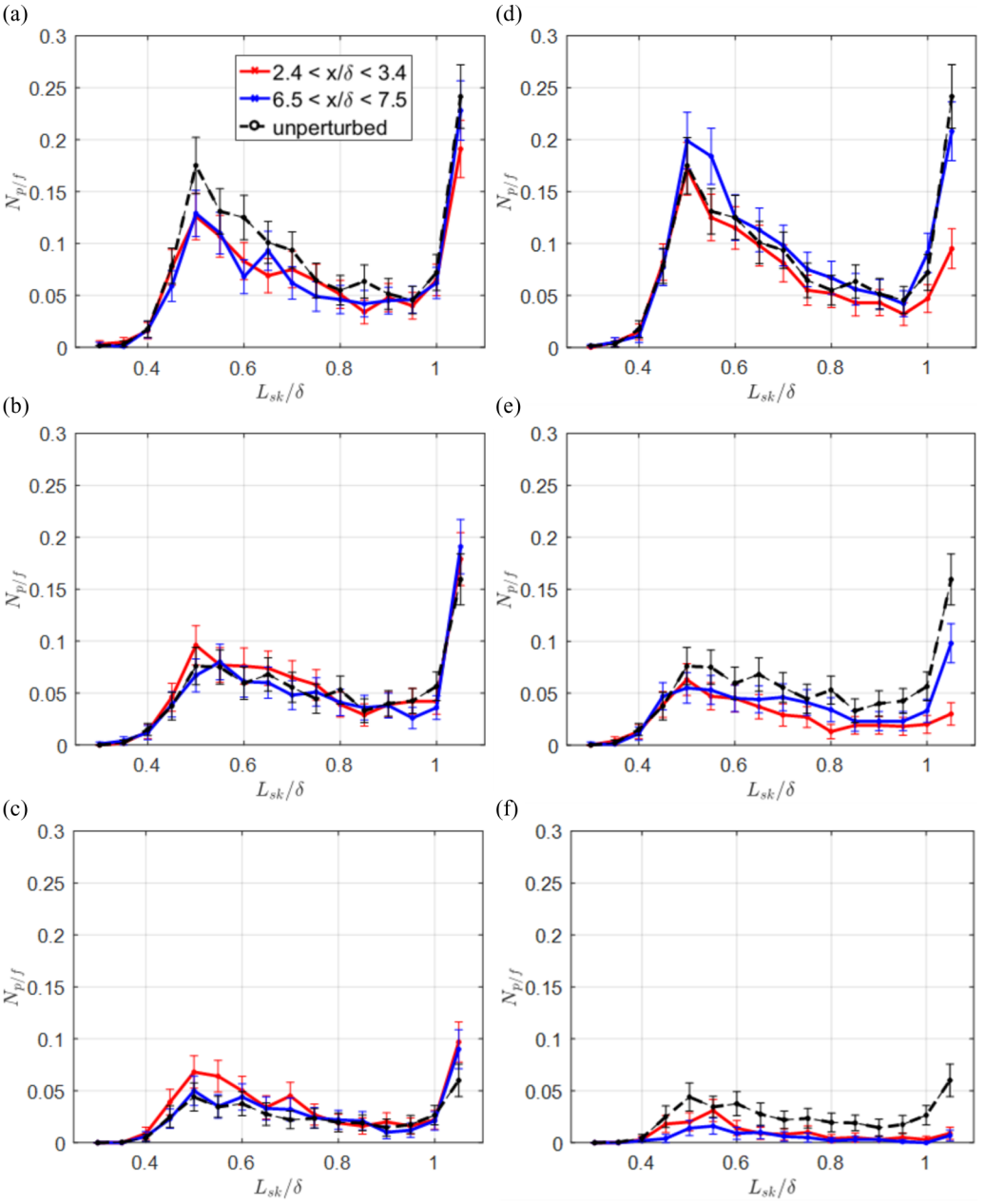

FIG. 14. Packet skeleton length histograms for flow downstream of $H = 0.2\delta$ array at (a) $z^+ = 125$, (b) $z^+ = 300$, and (c) $z^+ = 500$, and downstream of $H = \delta$ array at (d) $z^+ = 125$, (e) $z^+ = 300$, and (f) $z^+ = 500$. Histogram bin size $= 0.05\delta$.

hairpins or other vortices intersecting the wall-parallel plane. Note that this statistic is determined independent of the packet identification algorithm. As expected, the unperturbed swirl count was highest at $z^+ = 125$ and decreased with increasing measurement height. Immediately downstream of the cylinders, the number of swirls was increased at all measurement heights. At $z^+ = 125$ and 300, the values were similar, suggesting that identified swirling structures were likely dominated by

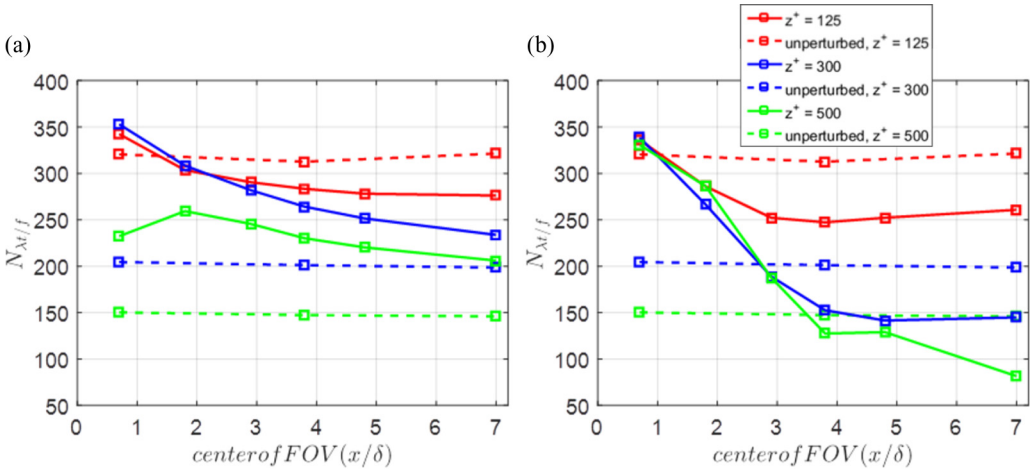

FIG. 15. Number of swirling structures per field downstream of (a) $H = 0.2\delta$ and (b) $H = \delta$ arrays.

Karman-like vortices shed from the cylinders. On the other hand, the increase in number of swirls at $z^+ = 500$ may be attributed to additional vortical structures generated at the cylinder tips. It is unclear how these structures might connect to the Karman-like structures below.

For $z^+ = 300$ and 500 in the perturbed flow, the trends in number of swirling structures [Fig. 15(a)] are very similar to those for RMS velocity in Fig. 9(b). At $z^+ = 300$, the number of swirls first sharply increased before declining toward the unperturbed value. At $z^+ = 500$, the number of swirls also increased significantly and peaked at $x = 1.8\delta$ before declining toward the unperturbed value as x continued to increase. The increase in swirl counts between $x = 0.7\delta$ and $x = 1.8\delta$ could potentially relate to upward extension of the Karman vortices forming below the tip height. At $z^+ = 125$, however, the number of swirling structures decreased below the unperturbed value already at $x = 1.8\delta$ and continued to decrease until $x = 7\delta$, where the value was 85% of the unperturbed value. At the same time, the RMS velocity never dropped below the unperturbed level. The decrease in number of swirls may be due to stretching or reorientation of pre-existing vortices, resulting in smaller swirl cross-sections. Furthermore, existing vortices may be weakened or eventually dissipated through interactions with surrounding structures. If the swirling cross sections are reduced, a number of vortices may still produce measurable velocity variations while becoming undetectable by the swirl identification algorithm. For a given PIV interrogation window size, the attenuation of velocity gradients will be stronger than the attenuation of velocity components [68].

In comparison, at $z^+ = 300$ and 500, the relative increases in number of swirls compared to the unperturbed flow at $x = 7\delta$ were 17% and 40%, respectively. The increased swirl counts were consistent with the result of Jacobi and McKeon [55] in a streamwise wall-normal plane, where additional swirling structures were observed at the top of the log layer, a distance 4δ downstream of a shorter perturbation ($H/\delta = 0.06$).

C. Flow perturbed by array with $H = \delta$

Compared with the $H = 0.2\delta$ case, significant differences were observed in the mean flow downstream of the taller $H = \delta$ array. Contours of mean streamwise velocity immediately downstream of the $H = \delta$ array are plotted in Fig. 16 for all measurement heights. Different from the $H = 0.2\delta$ case, velocity deficits were observed behind the $H = \delta$ cylinders at all measurement heights. Fast moving zones occurred between the cylinders. This spanwise pattern persists through the first data field, lasting until $x = 1.5\delta$ (not shown) at all measurement heights.

The variation of mean velocity averaged across the span downstream of the $H = \delta$ array is shown in Fig. 17(a). At $z^+ = 300$ and 500, the mean velocities decreased already by $x/d = 0.5$. By

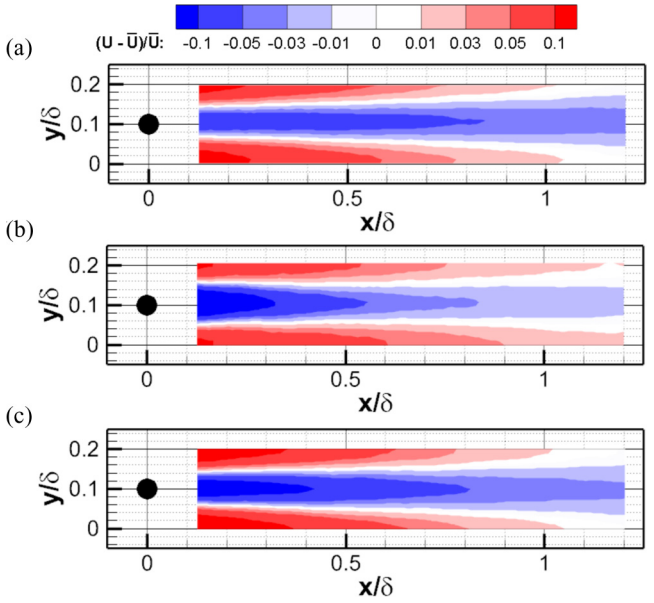

FIG. 16. Mean streamwise velocity downstream of flow perturbed by $H = \delta$ array at (a) $z^+ = 125$, (b) $z^+ = 300$, and (c) $z^+ = 500$.

contrast, the mean velocity at $z^+ = 125$ matched the unperturbed value initially, different from the $H = 0.2\delta$ case. (In the $H = \delta$ case the average velocity deficits immediately behind the cylinders at $z^+ = 125$ were weaker than those in the $H = 0.2\delta$ case, while the strength of the accelerated bleed flow through each array was the same.) The spanwise averaged results thus indicate that mean upwash related to the blockage from the much taller array was delayed initially in the region closer to the wall. At $z^+ = 125$, the mean streamwise velocity decreased steadily with increasing x until the end of the measurement domain where it was 6% less than the unperturbed value. This reduction was comparable to 5% reductions in $\bar{U}$ at $z^+ = 300$ and 500 and the same streamwise location. Thus, the $H = \delta$ array had a sustained effect on the mean velocity over a long distance.

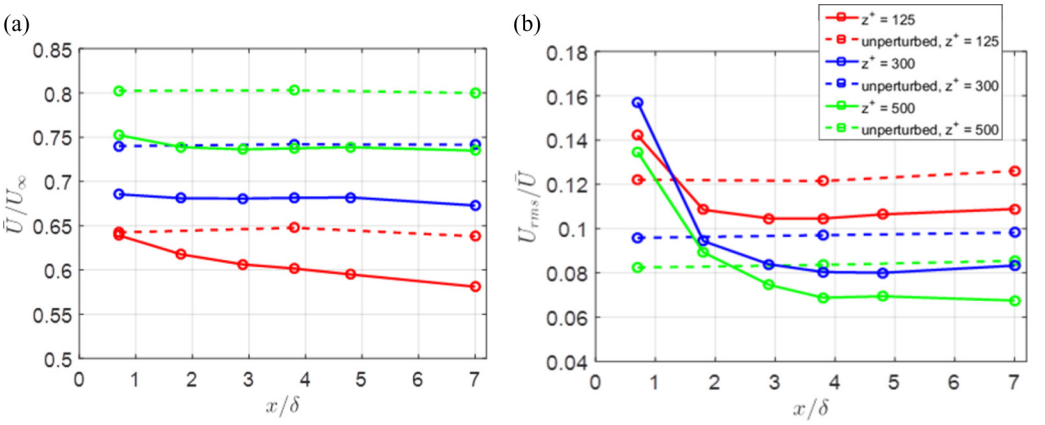

FIG. 17. Variation of (a) mean streamwise velocity normalized by free-stream velocity, and (b) root-mean square of streamwise velocity normalized with mean velocity at measurement height, with x location, downstream of the $H = \delta$ array.

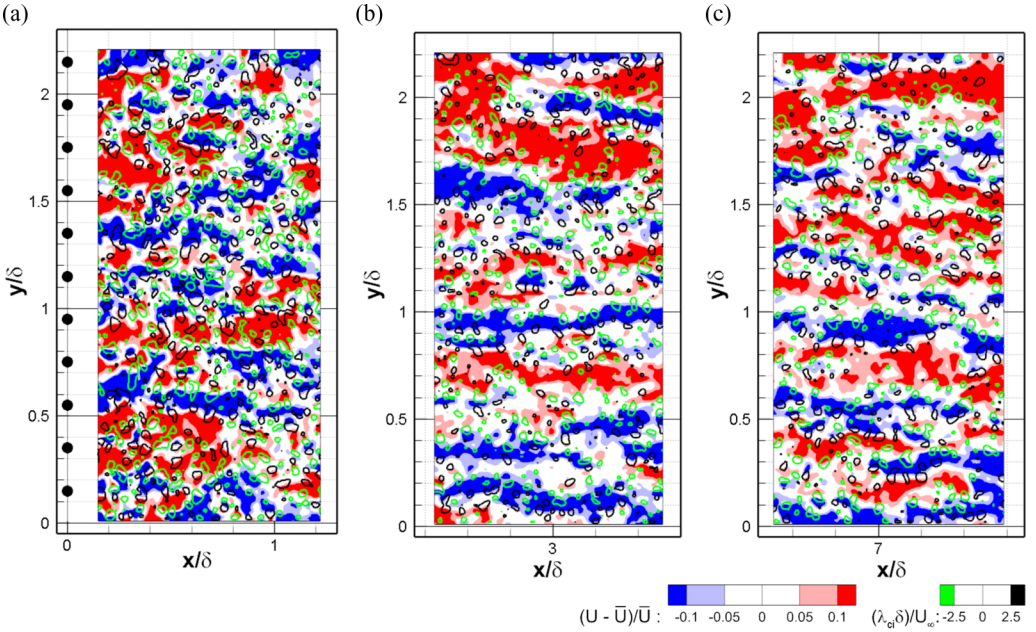

FIG. 18. PIV data of flow behind array with $H = \delta$ at $z^+ = 125$ centered at (a) $x = 0.7\delta$, (b) $x = 2.9\delta$, and (c) $x = 7\delta$.

This result was consistent with previous work by Corke *et al.* [42] and Lee *et al.* [50], albeit with perturbations different from those in the present study. Their results showed reductions in mean streamwise velocity within the log region compared to the unperturbed values at locations up to 9.3δ and 7.5δ downstream of their perturbations, respectively.

RMS velocity trends downstream of the two arrays were also different. Initially, the normalized RMS velocity downstream of the $H = \delta$ array [Fig. 17(b)] was increased at all measurement heights, similar to the $H = 0.2\delta$ case [see Fig. 9(b)]. However, for the $H = \delta$ array, the relative increase was strongest at $z^+ = 500$ and weakest at $z^+ = 125$. Moreover, different from the $H = 0.2\delta$ case, the initially increased RMS velocities downstream of the $H = \delta$ array decayed rapidly to levels below the unperturbed values, even when normalized by the reduced local mean velocities. The RMS velocity leveled off first at $z^+ = 125$ ($x/\delta = 2.9$), followed by $z^+ = 300$ and 500 at $x/\delta = 3.8$ and remained lower by $0.01\bar{U}$, 7δ downstream. A similar reduction in streamwise RMS velocity was observed by Boiko and Kornilov [48], Hutchins and Choi [49], and Corke *et al.* [42] within the log region of their perturbed boundary layers.

Instantaneous fields also revealed key differences between the flows downstream of the two arrays. For all three measurement heights, undulating wake structures were a dominant feature in the vicinity behind the $H = \delta$ array. At $z^+ = 125$ and 300, the wake structures were qualitatively similar to those observed downstream of the $H = 0.2\delta$ array even though the mean velocity statistics differed. The low momentum zones corresponding to wake structures often appeared short and very wavy. A few examples can be seen at $z^+ = 125$ [Fig. 18(a)], $y/\delta = 1.35$, at $z^+ = 300$ [Fig. 19(a)], $y/\delta = 0.3$ and $z^+ = 500$ [Fig. 20(a)], $y/\delta = 0.15$. Often, individual wakes would interact with adjacent ones, for example at $z^+ = 125$, $y/\delta = 1.35$ and 1.55, $z^+ = 300$, $y/\delta = 1.1$ and 1.3, and $z^+ = 500$, $y/\delta = 1.35$ and 1.55.

Remarkably, at $z^+ = 125$ and $x/\delta = 2.9$, the flow structures downstream of the $H = \delta$ array were relatively similar to those in unperturbed flow, and unlike the structures observed at the same location downstream of the $H = 0.2\delta$ array [compare Figs. 18(b) and 10(b) to unperturbed flow in Fig. 5(a)]. This similarity occurred in spite of the reduced mean velocity downstream of the $H = \delta$ array. For

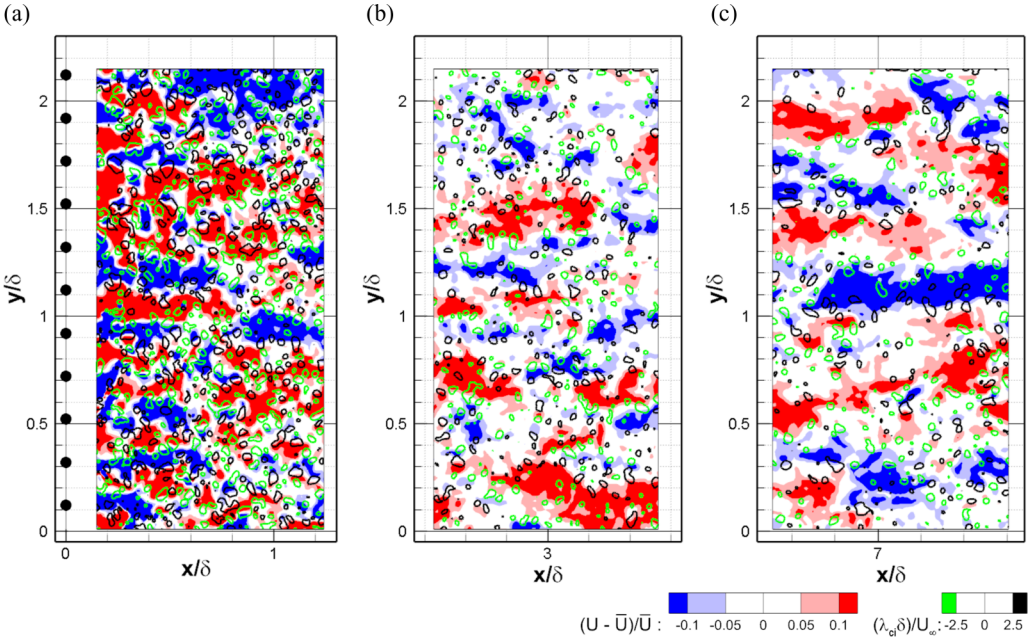

FIG. 19. PIV data of flow behind array with $H = \delta$ at $z^+ = 300$ centered at (a) $x = 0.7\delta$, (b) $x = 2.9\delta$, and (c) $x = 7\delta$.

the $H = \delta$ case, packets similar to those in the unperturbed flow were observed beginning at this streamwise location, as in Fig. 18(b) at $y/\delta = 0.15$, 0.3, 1.0, and 2.0. As x increased, the packet signatures became more similar to the packets in the unperturbed flow, such that they became less wavy and frequently longer than packet signatures upstream, for example, in Fig. 18(c) at $y/\delta = 0.3$, 0.5, 1.0, and 1.3.

At $z^+ = 300$ and 500, in contrast, packet signatures were hardly ever observed 2.9δ downstream of the $H = \delta$ array. The low momentum zones there often appeared disorganized, wavy, and short. Moreover, they were patchy with a dearth of obvious counter rotating swirls. Examples at $z^+ = 300$ [Fig. 19(b), $y/\delta = 0.7$, 1.2, and 1.8] and at $z^+ = 500$ [Fig. 20(b), $y/\delta = 0.7$ and 1.5] reflect this. At $x/\delta = 7$ and $z^+ = 300$, some packets similar to those in unperturbed flow were observable [e.g., at $y/\delta = 1.1$ in Fig. 19(c)]. In comparison, at $z^+ = 500$, packets similar to those in the unperturbed flow were hardly ever observed. Any packetlike structures tended to look narrower and shorter than those in the unperturbed flow. Examples can be seen in Fig. 19(c) at $y/\delta = 1.9$ and possibly 2.0. The flow organization here was substantially different from the flow downstream of the $H = 0.2\delta$ array [Fig. 12(c)].

The number of packets downstream of the array with $H = \delta$ is plotted in Fig. 13(b). The packet counts were reduced initially at all three measurement heights. This was different from the $H = 0.2\delta$ case, where the numbers increased initially at $z^+ = 300$ and 500 [see Fig. 13(a)]. At $z^+ = 125$, the number of packets in the flow perturbed by the $H = \delta$ array was 83% of the number in the unperturbed flow. With increasing x, the number of packets increased, exceeding the unperturbed packet count at $x = 4.8\delta$ and remaining slightly greater than the unperturbed value at $x = 7\delta$ (1.4 compared to 1.3), although this was within uncertainty. This was also different from the trend downstream of the $H = 0.2\delta$ array, where the packet count was reduced at $z^+ = 125$ for all streamwise locations.

For $H = \delta$, the packet counts at $z^+ = 300$ and 500 were 51% and 37% of the unperturbed values respectively at $x = 2.9\delta$. With increasing x, the number of packets at $z^+ = 300$ decreased to a minimum at $x = 3.8\delta$, then increased toward the unperturbed value with a shallower slope than the curve at $z^+ = 125$. In contrast, the number of packets at $z^+ = 500$ remain lower relative to

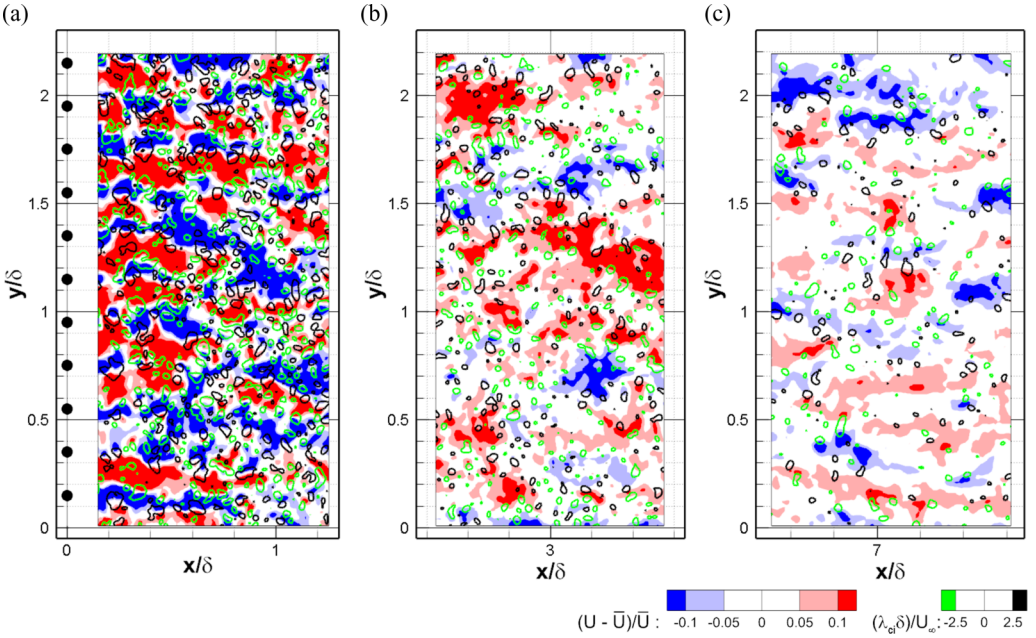

FIG. 20. PIV data of flow behind array with $H = \delta$ at $z^+ = 500$ centered at (a) $x = 0.7\delta$, (b) $x = 2.9\delta$, and (c) $x = 7\delta$.

the unperturbed value at all downstream locations with no indication of recovery. Packet counts at $z^+ = 300$ and 500 did not recover to the unperturbed value by $x = 7\delta$, remaining at 72% of the unperturbed packet count at $z^+ = 300$ and 22% at $z^+ = 500$.

Packet skeleton length histograms shown in Figs. 14(d)–14(f) indicate the effectiveness of the $H = \delta$ array at disrupting long packets, defined as packets with skeleton lengths greater than the field of view (1.05δ). The decrease in the number of long packets as a percentage of the unperturbed value was greatest at $z^+ = 500$ (90%), followed by $z^+ = 300$ (82%), and $z^+ = 125$ (60%). This effect was particularly evident in packet length histograms normalized by the respective number of packets detected at each measurement height. Normalized packet length distributions shifted towards shorter packets at all measurement heights at both $x = 2.9\delta$ and 7δ. However, the number of long packets increased substantially between 2.9δ and 7δ at both $z^+ = 125$ [Fig. 14(d)] and 300 [Fig. 14(e)] but only minimally at $z^+ = 500$.

The total number of swirls downstream of the $H = \delta$ array is shown in Fig. 15(b). Immediately downstream of the array, the swirl counts increased at all measurement heights compared to the unperturbed values. The number of swirls at all three measurement heights was similar and comparable to the numbers at $z^+ = 125$ and 300 for $H = 0.2\delta$ [see Fig. 15(a)]. Again, this collapse suggests that the number counts are dominated by swirls related to 2D vortex shedding in the near wake of each cylinder. Notably, the relative increase in number of swirls at $z^+ = 500$ was much greater at 2.2 times the unperturbed value compared to immediately downstream of the $H = 0.2\delta$ array [1.5 times unperturbed value in Fig. 15(a)]. Interestingly, the streamwise variations in swirl count downstream of the $H = \delta$ array [Fig. 15(b)] were similar to the trends in RMS velocity for all measurement heights [Fig. 17(b)], as was also true for $z^+ = 300$ and 500 in the $H = 0.2\delta$ array case.

With increasing x, the number of swirls downstream of the $H = \delta$ array decreased rapidly to levels below the unperturbed values at all measurement heights as occurred at $z^+ = 125$ for the $H = 0.2\delta$ case. Downstream of the $H = \delta$ array, the curve for $z^+ = 125$ encountered a minimum at $x = 3.8\delta$ before slightly increasing towards the unperturbed value with a shallow slope. At $x = 7\delta$, the number of swirls for $z^+ = 125$ was 80% of the unperturbed value. In contrast, at $z^+ = 300$

and 500, the number of swirls decreased continuously with increasing streamwise location. The curve at $z^+ = 300$ possibly encountered a minimum near $x = 4.8\delta$ and remained relatively flat until $x = 7\delta$. On the other hand, the curve for $z^+ = 500$ continued to decrease until $x = 7\delta$. At the final measurement location, the number of swirls measured was 72% and 54% of the unperturbed values at $z^+ = 300$ and 500, respectively.

IV. DISCUSSION AND CONCLUSIONS

Synthesis of the results highlights major differences in packet and boundary layer recovery downstream of the two arrays. The $H = \delta$ array generated profound perturbations across the entire boundary layer thickness. The blockage posed by this array led to significant upwash in the mean flow and consequently mean velocity deficits throughout the logarithmic region that lasted beyond the end of the measurement domain 7δ downstream of the perturbation. Although relative RMS velocities rose immediately downstream of the $H = \delta$ cylinders, they decreased rapidly with downstream distance, falling below unperturbed levels by $x = 2\delta$ and remaining lower until at least $x = 7\delta$. Immediately downstream of this array, wavy Karman-like wake patterns were prominent throughout the log region obscuring any obvious packet organization.

Starting at $x = 2.9\delta$, in spite of the strong perturbations to the mean and RMS velocity statistics, instantaneous velocity fields revealed packet signatures resembling those in the unperturbed flow appearing at $z^+ = 125$, the measurement location closest to the wall. At this wall-normal location, the number of packets identified by the algorithm increased with downstream distance, exceeding the unperturbed value at $x = 4.8\delta$ and continuing to increase until the end of the measurement domain. At $z^+ = 300$, packet signatures resembling those in the unperturbed flow became apparent further downstream, with the number identified by the algorithm beginning to increase after a minimum at $x = 3.8\delta$. At $z^+ = 500$, however, the strong reduction in number of packets was sustained until the end of the measurement domain.

Both the visualizations and the packet identification routine support the concept of a bottom-up mechanism for packet recovery. While the identification algorithm required a minimum packet length of 0.5δ, the number counts for packets longer than the field of view (1.1δ) in Figs. 12(d)–12(f) followed the same bottom-up recovery trend. The trends in the results are consistent with the initial streamwise growth and subsequent spanwise pairing mechanisms for packets proposed by Adrian *et al.* [1] and Tomkins and Adrian [23]. As characteristic scales of eddies close to the wall are smaller than those of eddies further away from the wall, it must take a longer distance for larger eddies away from the wall to develop and interact in order to return to the unperturbed state.

It is interesting that, at $z^+ = 125$ and $x = 7\delta$ for the $H = \delta$ case, the number of identified packet signatures exceeded the unperturbed value even though the relative RMS velocity and number of identified swirling structures remained reduced below the unperturbed values. These opposing trends indicate clearly that other boundary layer features unrelated to individual packets have not recovered to the unperturbed state. Nevertheless, the minimum in swirl count at $x = 2.9\delta$ corresponded directly to the streamwise location at which packets similar to those in the unperturbed flow were first observed and thus may be an indicator for initiation of recovery at this location. At $z^+ = 300$, a similar minimum occurred near $x/\delta = 4.8$, which was also consistent with the location where packets similar to those in the unperturbed flow were first observed. No minimum in swirl count was observed at $z^+ = 500$ as the number decreased continuously to the end of our measurement domain. This trend is another indicator of sustained disruption to the flow at $z^+ = 500$, consistent with the sustained disruption of packet signatures compared with those in the unperturbed flow.

The flow in the logarithmic region downstream of the $H = 0.2\delta$ ($H^+ = 500$) array revealed some significant differences in averaged statistics and packet recovery. The shorter cylinders also induced average velocity deficits associated with an initial mean upwash, but the deficits decreased with downstream distance implying subsequent mean downwash. In the measurement planes below the cylinder tip height, the relative RMS velocities first rose strongly as in the $H = \delta$ case, and at $z^+ = 500$, RMS values also increased. Unlike the $H = \delta$ case, however, the relative RMS values

decreased more slowly with increasing streamwise distance and remained elevated throughout the measurement domain (except for $z^+ = 125$, $x = 7\delta$, which relaxed to the unperturbed value).

Although visualizations and trends in packet counts suggested a top down approach to an unperturbed state as hypothesized by Zheng and Longmire [56], the overall picture was not so clear, because the flow structures in the region closest to the wall remained altered beyond the measurement domain. At $z^+ = 500$, which was the cylinder tip height, packets similar to those in the unperturbed flow existed throughout the streamwise domain as might be expected, consistent with the flying PIV measurements of Tan and Longmire [62]. At $z^+ = 300$, packet signatures were disrupted initially but reappeared starting near $x = 2.9\delta$. The number of packets identified at this location was slightly larger than in unperturbed flow, but the number relaxed to the unperturbed value by $x = 5\delta$.

Interestingly, the perturbations to the packet organization at $z^+ = 125$ appeared to last longer than in the $H = \delta$ case, even though the streamwise velocity statistics seemed to recover nearly to the unperturbed values. The number of packets identified at $x = 2.9\delta$ was 27% less than in unperturbed flow, and this value remained constant through the end of the measurement domain. Instantaneous visualizations showed that the large-scale flow organization at $x = 7\delta$ continued to differ from that in unperturbed flow in that signatures of spanwise merging or merged packet structures were much more frequent. Packet width distributions at this location (not shown) corroborate this observation, whereby the normalized distribution shifted towards larger widths (peak at 0.125δ) compared to those in unperturbed flow (peak at 0.075δ). On the other hand, width statistics for $z^+ = 300$ and 500 showed only minimal differences between perturbed and unperturbed cases. Therefore, the reason behind the reduced number of packets counted likely resulted from fewer "single width packets" that the algorithm was designed to identify. Further evidence for this argument was observed in the premultiplied energy spectrum for streamwise velocity at $z^+ = 125$, $x = 7\delta$ (see Ref. [66]), where energy was shifted from smaller to larger spanwise wavelengths compared with the unperturbed spectrum.

We suspect that the upwash and downwash and the related three-dimensional wake structures induced by the shorter cylinder array had a significant effect on the downstream flow and packet evolution. In addition to the results shown in Fig. 8, averaged volumetric results by Ortiz-Dueñas *et al.* [58] showed streamwise rollers immediately downstream of a similar array of $H = 0.2\delta$ ($H^+ = 500$) cylinders thought to be initiated by the cylinder tips. Flow is induced toward the wall directly behind each cylinder and away from the wall in the regions in between. Average wall-normal velocities were significant over the range $z^+ = 200$ to 500, and this effect persisted beyond $x = \delta$. In addition, stereoscopic PIV measurements in the log region at $x = 7\delta$ indicate increases in wall-normal RMS velocity compared to unperturbed flow. Thus, the persistence of enhanced wall-normal interactions across the log layer may have delayed the recovery of equilibrium-like or more canonical organization closer to the wall. These observations are consistent with those of Alving and Fernholz [69] and Rodríguez-López *et al.* [70,71] who examined a reattached boundary layer downstream of a separation and a boundary layer developing downstream of a wall-mounted sawtooth fence, respectively. In these studies, strong wall-normal interactions from recirculating fluid downstream of the separation and obstacle resulted in relatively slow recovery to the unperturbed state in the near-wall region. By contrast, downstream of two rows of relatively high aspect ratio cylinders more resemblant of our $H = \delta$ array, Rodríguez-López *et al.* [70] observed a weaker influence from the outer layer on the near wall region resulting in faster relaxation of the averaged near-wall flow statistics toward a canonical state.

Rodríguez-López *et al.* [70,71] ascribed the differences in boundary layer development between their two cases to wake-driven (sawtooth) and wall-driven (cylinders) mechanisms, respectively. Although the sawtooth fence had relatively larger blockage close to the wall and measurable separation downstream, unlike the current $H = 0.2\delta$ case, the sawtooth geometry implies that it must nevertheless initiate significant average streamwise vorticity in the near-wall region as occurs in the $H = 0.2\delta$ case. Our conclusion is thus that, even though the current $H = 0.2\delta$ and $H = \delta$ arrays present similar blockage and geometries beneath $z^+ = 500$, the enhanced outer/inner interactions

initiated near the tips of the shorter cylinders are sufficient to cause long-lasting disruptions to the vortex packet organization closer to the wall.

---

[1] R. J. Adrian, C. D. Meinhart, and C. D. Tomkins, Vortex organization in the outer region of the turbulent boundary layer, J. Fluid Mech. **422**, 1 (2000)

[2] D. J. C. Dennis and T. B. Nickels, Experimental measurement of large-scale three-dimensional structures in a turbulent boundary layer. Part 1. vortex packets, J. Fluid Mech. **673**, 180 (2011)

[3] A. Schröder, R. Geisler, K. Staack, G. E. Elsinga, F. Scarano, B. Wieneke, A. Henning, C. Poelma, and J. Westerweel, Eulerian and Lagrangian views of a turbulent boundary layer flow using time-resolved Tomographic PIV, Exp. Fluids. **50**, 1071 (2011)

[4] Y. Wu and K. T. Christensen, Population trends of spanwise vortices in wall turbulence, J. Fluid Mech. **568**, 55 (2006).

[5] Q. Gao, C. Ortiz-Dueñas, and E. K. Longmire, Analysis of vortex populations in turbulent wall-bounded flows, J. Fluid Mech. **678**, 87 (2011).

[6] Q. Gao, C. Ortiz-Dueñas, and E. K. Longmire, Evolution of coherent structures in turbulent boundary layers based on moving Tomographic PIV, Exp. Fluids. **54**, 1625 (2013).

[7] G. E. Elsinga, D. J. Kuik, B. W. van Oudheusden, and F. Scarano, Investigation of the three-dimensional coherent structures in a turbulent boundary layer with Tomographic-PIV, in *Proceedings of the 45th AIAA Aerospace Sciences Meeting and Exhibit, Reno, Nevada* (AIAA, Reston, VA, 2007).

[8] G. E. Elsinga, R. J. Adrian, B. W. van Oudheusden, and F. Scarano, Three-dimensional vortex organization in a high-Reynolds number supersonic turbulent boundary layer, J. Fluid Mech. **644**, 35 (2010).

[9] B. Ganapathisubramani, E. K. Longmire, and I. Marusic, Characteristics of vortex packets in turbulent boundary layers, J. Fluid Mech. **478**, 35 (2003).

[10] K. T. Christensen and R. J. Adrian, Statistical evidence of hairpin vortex packets in wall turbulence, J. Fluid Mech. **431**, 433 (2001)

[11] Y. Jodai and G. E. Elsinga, Experimental observation of hairpin auto-generation events in a turbulent boundary layer, J. Fluid Mech. **795**, 611 (2016).

[12] I. Marusic, On the role of large-scale structures in wall turbulence, Phys. Fluids **13**, 735 (2001).

[13] J. D. Woodcock and I. Marusic, The statistical behavior of attached eddies, Phys. Fluids **27**, 015104 (2015).

[14] C. M. de Silva, J. D. Woodcock, N. Hutchins, and I. Marusic, Influence of spatial exclusion on the statistical behavior of attached eddies, Phys. Rev. Fluids **1**, 022401(R) (2016).

[15] A. A. Townsend, *The Structure of Turbulent Shear Flows*, 2nd ed. (Cambridge University Press, Cambridge, 1976).

[16] A. E. Perry and M. S. Chong, On the mechanism of wall turbulence, J. Fluid Mech. **119**, 173 (1982).

[17] C. R. Smith, J. D. A. Walker, A. H. Haidari, and U. Sobrun, On the dynamics of near-wall turbulence, Phil. Trans. R. Soc. Lond. A **336**, 131 (1991).

[18] J. Zhou, R. J. Adrian, and S. Balachandar, Autogeneration of near-wall vortical structures in channel flow, Phys. Fluids **8**, 288 (1996).

[19] J. Zhou, R. J. Adrian, S. Balachandar, and T. M. Kendall, Mechanisms for generating coherent packets of hairpin vortices in channel flow, J. Fluid Mech. **387**, 353 (1999).

[20] K. Kim, H. J. Sung, and R. J. Adrian, Effects of background noise on generating coherent packets of hairpin vortices, Phys. Fluids **20**, 105107 (2008).

[21] C. E. Wark and H. M. Nagib, Relation between outer structure and wall layer events in boundary layers with and without manipulation, in *Structure of Turbulence and Drag Reduction*, edited by A. Gyr (Springer-Verlag, Berlin, 1990).

[22] R. J. Adrian, S. Balachandar, and Z. C. Lin, Spanwise growth of vortex structure in wall turbulence, KSME Int. J. **15**, 1741 (2001).

[23] C. D. Tomkins and R. J. Adrian, Spanwise structure and scale growth in turbulent boundary layers, J. Fluid Mech. **490**, 37 (2003).

[24] C. D. Tomkins and R. J. Adrian, Energetic spanwise modes in the logarithmic layer of a turbulent boundary layer, J. Fluid Mech., **545**, 141 (2005).
[25] N. Hutchins and I. Marusic, Evidence of very long meandering features in the logarithmic region of turbulent boundary layers, J. Fluid Mech **579**, 1 (2007).
[26] R. Mathis, N. Hutchins, and I. Marusic, Large-scale amplitude modulation of the small-scale structures in turbulent boundary layers, J. Fluid Mech. **628**, 311 (2009)
[27] R. Mathis, I. Marusic, N. Hutchins, and K. R. Sreenivasan, The relationship between the velocity skewness and the amplitude modulation of the small scale by the large scale in turbulent boundary layers, Phys. Fluids **23**, 121702 (2011).
[28] B. Ganapathisubramani, N. Hutchins, J. P. Monty, D. Chung, and I. Marusic, Amplitude and frequency modulation in wall turbulence, J. Fluid Mech. **712**, 61 (2012).
[29] L. Agostini and M. A. Leschziner, On the influence of outer large-scale structures on near-wall turbulence in channel flow, Phys. Fluids **26**, 075107 (2014).
[30] D. W. Bechert, M. Bruse, W. Hage, J. G. T. Van Der Hoeven, and G. Hoppe, Experiments on drag-reducing surfaces and their optimization with an adjustable geometry, J. Fluid Mech. **338**, 59 (1997).
[31] S. E. Belcher, N. Jerram, and J. C. R. Hunt, Adjustment of a turbulent boundary layer to a canopy of roughness elements, J. Fluid Mech. **488**, 369 (2003).
[32] J. Jiménez, Turbulent flows over rough walls, Annu. Rev. Fluid Mech. **36**, 173 (2004).
[33] Y. Wu and K. T. Christensen, Spatial structure of a turbulent boundary layer with irregular surface roughness, J. Fluid Mech. **655**, 380 (2010).
[34] B. Nugroho, N. Hutchins, and J. P. Monty, Large-scale spanwise periodicity in a turbulent boundary layer induced by highly ordered and directional surface roughness, Int. J. Heat Fluid Flow, **41**, 90 (2013).
[35] K. A. Flack and M. P. Schultz, Roughness effects on wall-bounded turbulent flows, Phys. Fluids **26**, 101305 (2014).
[36] O. Coceal, A. Dobre, T. G. Thomas, and S. E. Belcher, Structure of turbulent flow over regular arrays of cubical roughness, J. Fluid Mech. **589**, 375 (2007).
[37] I. P. Castro, H. Cheng, and R. Reynolds, Turbulence over urban-type roughness: Deductions from wind tunnel measurements, Boundary-Layer Meteorol. **118**, 109 (2006).
[38] J. P. Monty, J. J. Allen, K. Lien, and M. S. Chong, Modification of the large-scale features of high Reynolds number wall turbulence by passive surface obtrusions, Exp. Fluids **51**, 1755 (2011).
[39] C. Vanderwel and B. Ganapathisubramani, Effects of spanwise spacing on large-scale secondary flows in rough-wall turbulent boundary layers, J.Fluid Mech. **774**, R2 (2015).
[40] R. J. Volino, M. P. Schultz, and K. A. Flack, Turbulence structure in rough and smooth wall boundary layers, J. Fluid Mech. **592**, 263 (2007).
[41] D. T. Squire, C. Morill-Winter, N. Hutchins, M. P. Schultz, J. C. Klewicki, and I. Marusic, Comparison of turbulent boundary layers over smooth and rough surfaces up to high Reynolds numbers, J. Fluid Mech. **795**, 210 (2016).
[42] T. C. Corke, Y. Guezennec, and H. M. Nagib, Modification in drag of turbulent boundary layers resulting from manipulation of large-scale structures, NASA CR 3444 (1981).
[43] J. N. Hefner, J. B. Anders, and D. M. Bushnell, Alteration of outer flow structures for turbulent drag reduction, AIAA J. 83–0193 (1983).
[44] A. M. Savill and J. C. Mumford, Manipulation of turbulent boundary layers by outer-layer devices: skin-friction and flow-visualization results, J. Fluid Mech. **191**, 389 (1988).
[45] M. W. Plesniak and H. M. Nagib, Net drag reduction in turbulent boundary layers resulting from optimized manipulation, in *Proceedings of the AIAA Shear Flow Control Conference, Boulder, CO, March 12–14 1985*, Paper No. AIAA-85-0518 (AIAA, Reston, VA, 1985).
[46] C. E. Wark, M. A. Naguib, and H. M. Nagib, Effect of plate manipulators on coherent structures in a turbulent boundary layer, AIAA J. 28–1877 (1990).
[47] S. P. Wilkinson, J. B. Anders, B. S. Lazos, and D. M. Bushnell, Turbulent drag reduction research at NASA Langley—Progress and plans, Int. J. Heat Fluid Flow **9**, 266 (1988).
[48] A. V. Boiko and V. I. Kornilov, On the vertical large eddy breakup device capability to decrease the turbulent drag, Thermophys. Aeromech. **16**, 549 (2009).

[49] N. Hutchins and K. S. Choi, Towards a greater understanding of turbulent skin friction reduction, in *Proceedings of ASME Fluid Engineering Conference, Montreal, Quebec, Canada* (ASME, 2002).
[50] S. J. Lee and H. B. Kim, Laboratory measurements of velocity and turbulence field behind porous fences, J. Wind Eng. Industr. Aerodynam. **80**, 311 (1999).
[51] H. Sakamoto and M. Arie, Vortex shedding from a rectangular prism and a circular cylinder placed vertically in a turbulent boundary layer, J. Fluid Mech. **126**, 147 (1983).
[52] W. H. Schofield and E. Logan, Turbulent shear flow over surface mounted obstacles, J. Fluid Eng. **112**, 376 (1990).
[53] C. D. Tomkins, The structure of turbulence over smooth and rough walls, Ph.D thesis, University of Illinois at Urbana Champaign, 2001.
[54] M. Guala, C. D. Tomkins, K. T. Christensen, and R. J. Adrian, Vortex organization in a turbulent boundary layer overlying sparse roughness elements, J. Hydraulic Res. **50**, 465 (2012).
[55] I. Jacobi and B. J. McKeon, New perspectives on the impulsive roughness-perturbation of a turbulent boundary layer, J. Fluid Mech. **677**, 179 (2011).
[56] S. Zheng and E. K. Longmire, Perturbing vortex packets in a turbulent boundary layer, J. Fluid Mech. **748**, 368 (2014)
[57] M. D. Ryan, C. Ortiz-Dueñas, and E. K. Longmire, Effects of simple wall-mounted cylinder arrangements on a turbulent boundary layer, AIAA J. **49**, 2210 (2011)
[58] C. Ortiz-Dueñas, M. D. Ryan, and E. K. Longmire, Modification of turbulent boundary layer structure using immersed wall- mounted cylinders, in *Proceedings of the Conference on Turbulent Shear Flow Phenomena VIII, Ottawa* (2011).
[59] J. Lin, J. P. Laval, J. M. Foucaut, and M. Stanislas, Quantitative characterization of coherent structures in the buffer layer of near-wall turbulence. Part 1: Streaks, Exp. Fluids. **45**, 999 (2008).
[60] J. H. Lee and H. J. Sung, Very-large-scale motions in a turbulent boundary layer, J. Fluid Mech. **673**, 80 (2011).
[61] K. P. Nolan and T. A. Zaki, Conditional sampling of transitionary boundary layers in pressure gradients, J. Fluid Mech. **728**, 306 (2013)
[62] Y. M. Tan and E. K. Longmire, On the re-organization of perturbed hairpin packets in a turbulent boundary layer, in *Proceedings of the 11th International Symposium on Particle Image Velocimetry, Santa Barbara, CA* (2015).
[63] Q. Gao, Evolution of eddies and packets in turbulent boundary layers, Ph.D thesis, University of Minnesota, 2011.
[64] D. Sumner, J. L. Heseltine, and O. J. P. Dansereau, Wake structure of a finite circular cylinder of small aspect ratio, Exp Fluids. **37**, 720 (2004).
[65] C. W. Park and S. J. Lee, Free end effects on the near wake flow structure behind a finite circular cylinder, J. Wind Eng. Industr. Aerodynam. **88**, 231 (2000).
[66] Y. M. Tan, Turbulent boundary layers perturbed by an array of cylinders, Ph.D thesis, University of Minnesota, 2017.
[67] J. A. Sillero, J. Jiménez, and R. D. Moser, One-point statistics for turbulent wall-bounded flows at Reynolds numbers up to $\delta^+ \sim 2000$, Phys. Fluids **25**, 105102 (2013).
[68] N. Saikrishnan, I. Marusic, and E. K. Longmire, Assessment of dual plane PIV measurements in wall turbulence using DNS data, Exp Fluids. **41**, 265 (2006).
[69] A. E. Alving and H. H. Fernholz, Turbulence measurements around a mild separation bubble and downstream of reattachment, J. Fluid Mech. **322**, 297 (1996).
[70] E. Rodríguez-López, P. J. K. Bruce, and O. R. H. Buxton, Near field development of artificially generated high Reynolds number turbulent boundary layers, Phys. Rev. Fluids **1**, 074401 (2016).
[71] E. Rodríguez-López, P. J. K. Bruce, and O. R. H. Buxton, On the formation mechanisms of artificially generated high Reynolds number turbulent boundary layers, Boundary-Layer Meteorol. **160**, 201 (2016).